Nanoscale imaging of molecular positions and anisotropies

Travis J Gould[1,5], Mudalige S Gunewardene[1,5], Manasa V Gudheti[1], Vladislav V Verkhusha[2], Shu-Rong Yin[3], Julie A Gosse[4] & Samuel T Hess[1]

Knowledge of the orientation of molecules within biological structures is crucial to understanding the mechanisms of cell function. We present a method to image simultaneously the positions and fluorescence anisotropies of large numbers of single molecules with nanometer lateral resolution within a sample. Based on a simple modification of fluorescence photoactivation localization microscopy (FPALM), polarization (P)-FPALM does not compromise speed or sensitivity. We show results for mouse fibroblasts expressing Dendra2-actin or Dendra2-hemagglutinin.

Light microscopy allows noninvasive imaging of multiple species in biological specimens with single-molecule sensitivity, but diffraction normally limits the resolution to ~150–250 nm. As many biological processes occur on smaller length scales, techniques that can image below the diffraction limit and yield single-molecule information are becoming increasingly important.

Recently developed methods can break the diffraction barrier by stimulated emission depletion[1] or by localization of large numbers of single molecules, and achieve effective resolution in the 10–40 nm range[2–4]. In localization-based methods, small subsets of photoactivatable fluorescent molecules are stochastically activated in the sample by illumination with an activation laser. Photoactivated molecules are illuminated by a second laser, imaged and then deactivated, either actively or by spontaneous photobleaching. The process is repeated until data have been acquired on a sufficiently large number of molecules or all possible molecules. Image analysis is then used to measure the position of each molecule and determine its intensity.

Localization-based methods can now image living cells[5,6], three-dimensional specimens[7,8] and multiple species. These methods, however, do not provide information about the orientation and rotational freedom of individual molecules, which can be used to test the degree of interaction between molecules in biological systems. Furthermore, understanding organization and functionality of molecular machines often requires determination of the orientation of molecules within cellular structures and relative to one another. Previous imaging of single molecule anisotropies has relied on near-field methods[9], shape analysis of molecular images obtained by diffraction-limited techniques[10,11] or other methods of imaging relatively sparse distributions of molecules. We set out to augment the capabilities of localization-based microscopy to obtain high-density maps of single-molecule positions and anisotropies.

We present a method for imaging single-molecule polarization anisotropy (a measure of the orientation of the transition dipole moment of a fluorescent molecule) in biological specimens with resolution below the diffraction limit. Our method is based on fluorescence photoactivation localization microscopy (FPALM)[2] with a modified detection path, and we termed it polarization-FPALM (P-FPALM). The addition of a polarizing beam splitter into the detection path allows simultaneous, spatially separate imaging of the emission polarized parallel and perpendicular to a particular axis within the sample. The two detection paths are adjusted to have the same total length from the microscope tube lens. Analysis of the relative intensities of molecules in the two images yields the anisotropy of each localized molecule. Others have implemented a similar approach to study the rotational mobility of individual fluorescent molecules during single-particle tracking experiments[12].

For imaging, we placed the sample on the stage of an inverted microscope with a ×60, 1.2 numerical aperture (NA) water-immersion objective and illuminated it using two lasers: 405 nm activation and 488 nm readout for the photoactivatable green fluorescent protein (PA-GFP)[13] or 405 nm activation and 556 nm readout for the photoswitchable protein Dendra2 (ref. 14), which can be photoactivated from a green-fluorescent form to a red-fluorescent form. We focused the lasers in the objective back-aperture to cause a large area of the sample to be illuminated with an approximately Gaussian profile with linear polarization along the *x*, *x* and *y* directions for the 405, 488 and 556 nm beams, respectively (**Supplementary Figs. 1** and **2** online). Fluorescence detected by the same objective is filtered by the dichroic mirror and interference filters (**Supplementary Table 1** online), focused by the tube lens to form an intermediate image, which is magnified by a telescope consisting of +60 mm and +200 mm achromatic lenses, to result in an overall magnification of ~192 and an effective pixel size in object space of 83.3 nm. The magnified image was detected with an electron-multiplying charge-coupled device (EMCCD) camera at 10–32 frames per second for ~20–600 s (**Supplementary Table 2** online). The use of a water-immersion lens is an

[1]Department of Physics and Astronomy and Institute for Molecular Biophysics, 5709 Bennett Hall, University of Maine, Orono, Maine 04469, USA. [2]Department of Anatomy and Structural Biology, Albert Einstein College of Medicine, 1300 Morris Park Avenue, Bronx, New York 10461, USA. [3]Laboratory for Cellular and Molecular Biophysics, Program in Physical Biology, National Institute of Child Health and Human Development, 10 Center Drive, Bethesda, Maryland 20892, USA. [4]Department of Biochemistry, Microbiology, and Molecular Biology, 5735 Hitchner Hall, University of Maine, Orono, Maine 04469, USA. [5]These authors contributed equally to this work. Correspondence should be addressed to S.T.H. (sam.hess@umit.maine.edu).

RECEIVED 4 JUNE; ACCEPTED 22 OCTOBER; PUBLISHED ONLINE 16 NOVEMBER 2008; DOI:10.1038/NMETH.1271

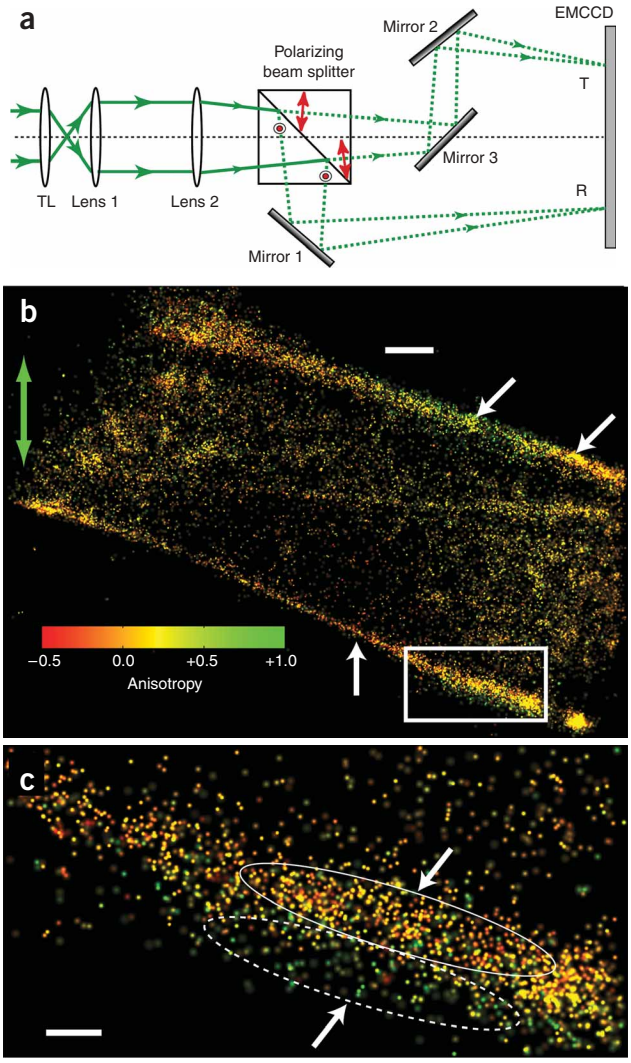

Figure 1 | P-FPALM detection path and P-FPALM imaging of a fixed fibroblast expressing Dendra2-actin. (**a**) The intermediate image formed by tube lens (TL) is expanded by lenses 1 and 2 before entering the polarizing beam splitter. The reflected beam (R; lower path, light polarized in the *x* direction at the sample) is directed to the EMCCD by mirror 1 while the transmitted beam (T; upper path, light polarized in the *y* direction at the sample) is directed to the same EMCCD by mirrors 2 and 3. Mirrors 2 and 3 are adjusted so that the total length of both paths is equal. Red arrows and circles show the polarization of the light in the T and R paths, respectively. (**b**) P-FPALM image of Dendra2-actin expressed in a fixed fibroblast (21,525 molecules). Green arrow indicates the direction of polarization of the readout beam. (**c**) Magnification of the boxed region in **b**. Gradients in single-molecule anisotropy (2,015 molecules) are marked by arrows and ellipses. White arrows in **b** and **c** point to regions within the cell with consistently negative or consistently positive anisotropy values. Compare for example the two regions marked by arrows on the upper right of **b**. Compare also the lower fiber bundle in **b** labeled with the arrow, and the regions outlined by ellipses in **c**. Color bar indicates anisotropy scale for **b** and **c**. Scale bars, 1 μm (**b**) and 250 nm (**c**).

advantage because it minimizes aberrations when imaging a sample that is also in water. Illumination using a relatively unfocused Gaussian beam is also advantageous because it reduces the tipping of the polarization toward the *z* axis, which results from a high-NA diffraction-limited focus. Because single molecules are being localized using two detection channels (three channels are required to determine the full orientation in three dimensions), anisotropies measured for molecules that are oriented with a component out of the *x*-*y* plane will only be approximate, owing to tipping of the polarization by the high-NA objective[15]. As a result, the anisotropies we acquired could not be interpreted directly as an angle relative to the laser polarization axis, but calculations accounting for the effects of polarization tipping (**Supplementary Figs. 3** and **4** online) allowed specification of the range of orientations the molecule could have (**Supplementary Fig. 5** online), within experimental error, when close to the center of the field. Activation and illumination pulse protocols are described in **Supplementary Methods** and **Supplementary Table 2** online.

For analysis, the images T and R (**Fig. 1a** and **Supplementary Fig. 1**), corresponding to the fluorescence transmitted and reflected by the polarizing beamsplitter, respectively, are first correlated with each other using images of fluorescent beads. Image R is shifted, rotated, and stretched linearly in the *x* and *y* directions (conserving the total number of detected photons), to produce the best normalized cross-correlation with image T. The transformation parameters measured from the bead images are then used to transform all subsequent images.

We calculated the anisotropy (r) from the ratio of fluorescence emitted by the molecule and detected with polarization parallel ($I_{||}$) and perpendicular ($I_{\perp}$) to the laser, respectively[16]:

$$r = \frac{I_{||} - I_{\perp}}{I_{||} + 2I_{\perp}} \quad (1)$$

The $I_{||}$ and $I_{\perp}$ were background subtracted, and corrected for bleed-through and relative detection efficiency (see **Supplementary Methods** for details on experimental methods and comparison with simulations). As a control, we determined mean anisotropy values for rhodamine B in both low- and high-viscosity solutions; these values agreed within uncertainty (±0.025 in anisotropy value) with results published previously[17], demonstrating the accuracy of the method on a sample with known anisotropy values (**Supplementary Fig. 6a** online). Anisotropies measured for caged-fluorescein suspended in agarose gel also agreed with theoretical calculations (**Supplementary Fig. 7** online).

PA-GFP molecules imaged on glass showed little spatial dependence of the anisotropy (**Supplementary Fig. 8** online). In contrast, molecules localized in cells transfected with Dendra2-actin had elongated filamentous structures with clear patterns in the distribution and anisotropy values of molecules (**Fig. 1b**,**c** and **Supplementary Fig. 9** online). We expected actin fiber bundle density to affect the measured anisotropy by limiting or permitting certain probe orientations.

The effective resolution (**Supplementary Methods**, equation S3) of ~26 nm calculated for the structure shown in **Figure 1c** was limited by the localization precision (~7 nm median value; **Supplementary Fig. 10** online), but more so by the density of localized molecules (~25 nm median nearest neighbor distance). We improved the localization precision compared to our previous FPALM work by reducing background by prebleaching imaging buffers with UV light, using a lower-noise camera and increasing the excitation intensity. Also, consistent with other reports in the field, we report the one-sigma uncertainty in positions using the s.d. of the point spread function (**Supplementary Methods**, equation S1), rather than the $1/e^2$ radius of the point spread function we used previously[5]. The reported localization precision

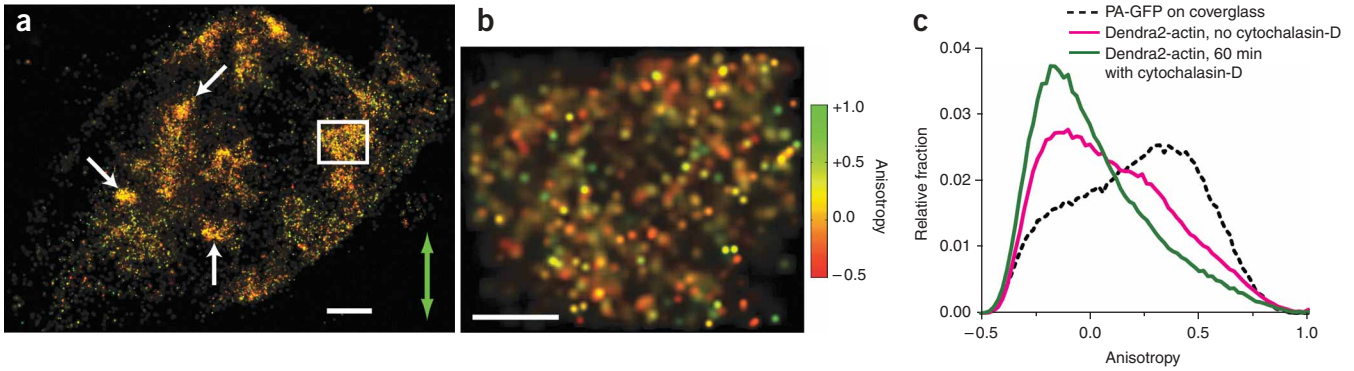

Figure 2 | Effect of cytochalasin-D on structure and anisotropy of Dendra2-actin. (**a**) P-FPALM image of a fixed fibroblast after a 60-min treatment with 1 μM cytochalasin-D (32,553 molecules). Green arrow indicates the direction of polarization of the readout beam. White arrows indicate globular clusters of Dendra2-actin. (**b**) Magnification of the boxed region in **a** (1,878 molecules) highlighting a mixture of molecules emitting parallel and perpendicular to the excitation. Color bar indicates anisotropy scale in **a** and **b**. Scale bars, 1 μm (**a**) and 250 nm (**b**). (**c**) Cumulative distribution of single-molecule anisotropies for PA-GFP on coverglass ($n = 10$; 108,399 total molecules), and in fixed fibroblasts expressing Dendra2-actin without cytochalasin-D treatment ($n = 30$; 496,844 total molecules) and after a 60-min treatment with 1 μM cytochalasin-D ($n = 5$; 187,457 total molecules).

values had been calculated from measured numbers of photons, and do not take into account other sources of uncertainty, such as drift and detector heterogeneity. Under the criterion for effective resolution given in reference 6, where twice the nearest neighbor distance had been used as a measure of the Nyquist limit, the effective resolution for the data in **Figure 1c** would be ~50 nm.

Molecules localized in the extended fiber bundles had obvious gradients in their anisotropy; some regions contained mostly molecules emitting parallel to the direction of the excitation (**Fig. 1b**,**c**). In another region within the same structure, the majority of molecules emitted fluorescence polarized perpendicular to the excitation direction (**Fig. 1b**). We observed the opposite trend in anisotropy close to the edge of the cell (**Fig. 1b**,**c**). In contrast, the interior of the cell had fewer visible fiber bundles but instead had actin-rich regions >1 μm wide without extended linear structures (**Supplementary Fig. 9b**), resembling actin imaged by PALM in lamellipodia[3]. Confocal images of cells labeled with both Dendra2-actin and Alexa-680–phalloidin confirmed co-localization of Dendra2-actin with actin structures (**Supplementary Fig. 11** online).

To test whether these trends in anisotropy correspond to filamentous actin structures, we treated cells with 1 μM cytochalasin-D for 60 min to disrupt the actin cytoskeleton before fixing and imaging them. The cell structure changed drastically (**Figs. 2a**,**b** and **Supplementary Figs. 12** and **13** online): the cells rounded up, the fiber bundles were no longer visible, and the remaining structures showed very little trend in the anisotropy. Among all treated cells that we imaged, none showed distinct filamentous structures or anisotropy patterns like the ones observed in untreated cells. Within the ~1 μm-sized globular clusters that were visible, we observed a mixture of molecules emitting parallel and perpendicular to the excitation (**Fig. 2b**). Overall histograms of anisotropy values for all treated and all untreated cells showed substantial differences resulting from cytochalasin-D treatment (**Fig. 2c** and **Supplementary Fig. 14** online). Note that all structures visible below ~250 nm would be unresolved in a conventional fluorescence microscope.

When interpreting anisotropy values, probe rotational mobility is an important consideration. Even in fixed samples, fluorescent probes not attached to cell structures by multiple fixative cross-links may be capable of limited motion. Because the rotational time constant for fluorescent proteins in cells[18] is typically on the nanosecond timescale, the emission from a given orientation of the probe will be sampled thousands of times during a single frame. Hence, the measured anisotropy will reflect the range of orientations accessible to the probe. For fixed samples, fewer orientations will be accessible, and the anisotropy values will be substantially different from the values observed for freely diffusing molecules in solution[16].

To evaluate P-FPALM using a different biological application we obtained images of hemagglutinin in fixed fibroblasts. This yielded clustered distributions of hemagglutinin consistent with previous FPALM imaging[7] and also provided orientational information for individual hemagglutinin molecules within clusters. The anisotropy of PA-GFP–tagged hemagglutinin showed an example of a cluster of molecules with similar anisotropy values, positioned near the edge of the cell, approximately ~1 × 2 μm in size (**Supplementary Fig. 15** online). The surrounding clusters of molecules had larger values of anisotropy. P-FPALM imaging of Dendra2-tagged hemagglutinin (**Supplementary Figs. 16** and **17** online) also showed hemagglutinin clustering. In some cases, we observed differences in anisotropy values from cluster to cluster. Whereas anisotropy measurements of some tagged molecules could be tag-dependent, we neither confirmed nor excluded this possibility. These spatially dependent differences in anisotropy could be useful for understanding the formation of clusters of hemagglutinin in membranes, which are used by the influenza virus to gain entry into host cells and to assemble the components to build a new virus that will eventually bud from the host cell.

The ability to image the anisotropy with resolution below the diffraction limit presents several captivating opportunities, most importantly the ability to image short-range order and to quantify the degree of preferential orientation of molecules. As long as the limitations of the method are taken into account, we can use the anisotropy to estimate the degree of alignment (but not the precise angle) between the transition-dipole moment of the emitting molecule (the fluorescent probe) and a particular coordinate axis[16]. Interactions between membrane domains and the cytoskeleton, such as those found in focal adhesions[6], are expected to result in preferential orientation of molecules, but the size of those

structures is generally well below the diffraction limit[19]. The improved resolution in P-FPALM will allow quantification of order of proteins and lipids in membrane domains at length scales inaccessible to standard methods.

The ability to image both nanoscale structure and quantify relative molecular orientation can address biological questions where improved resolution is crucial but insufficient by itself. In principle, P-FPALM will be compatible with live-cell FPALM, with PALM and STORM using widefield excitation, and with multicolor imaging. It requires only the addition of a polarizing beam splitter, three mirrors and two lenses to the original FPALM geometry. Detection efficiency is not substantially reduced.

In future live-cell applications, the anisotropy could be used to distinguish between molecules that are bound and unbound: for example, a ligand that binds a membrane receptor will not sample all orientations and will in some cases show greater anisotropy than an unbound copy of the same molecule. This kind of approach will be useful for studies of protein-protein interactions, polymerization, depolymerization, growth and collapse of intracellular structures, and lateral organization in membranes. As high excitation intensities are potentially damaging to cells, users of P-FPALM will certainly need to make appropriate control experiments to check for any effects of the high intensity illumination on cell viability.

Longer acquisitions may allow higher molecular densities to be observed in well-immobilized samples. Extension of the technique to three-dimensional imaging would be both possible and useful, considering that structures such as actin will span many focal planes. Hence, three-dimensional imaging would capture larger numbers of total molecules in different focal planes and allow extended structures to be visualized even more comprehensively. P-FPALM takes advantage of the information encoded in the polarization of light to show the first nanoscale images of the orientations of molecules within biological structures.

Note: Supplementary information is available on the Nature Methods website.

ACKNOWLEDGMENTS

We thank C. Fang-Yen, P. Blank, J. Bewersdorf, J. Zimmerberg and M. Mason for useful discussions, G. Patterson (US National Institute of Child Health and Human Development) for providing the construct encoding the PA-GFP protein, J. Shim, J. Rochira and E. Allgeyer for laboratory assistance, A. McGinn, T. Tripp and P. Byard for professional services. This work was supported by grants K25-65459 from the US National Institute of Allergy and Infectious Diseases, CHE-0722759 from the National Science Foundation, start up funds from the University of Maine (S.T.H.), and by grants GM070358 and GM073913 from the National Institute of General Medical Sciences (V.V.V.).

AUTHOR CONTRIBUTIONS

T.J.G. and M.S.G. conceived the method, performed and analyzed experiments, wrote and edited the manuscript. M.V.G. performed experiments and edited the manuscript. V.V.V. and S.-R.Y. created genetic constructs and edited the manuscript. J.A.G. assisted with experiments and analysis, and edited the manuscript. S.T.H. conceived the method, performed and analyzed experiments, wrote and edited the manuscript.

COMPETING INTERESTS STATEMENT

The authors declare competing financial interests: details accompany the full-text HTML version of the paper at http://www.nature.com/naturemethods/.

Published online at http://www.nature.com/naturemethods/
Reprints and permissions information is available online at http://npg.nature.com/reprintsandpermissions/

1. Hell, S.W. & Wichmann, J. *Opt. Lett.* **19**, 780–782 (1994).
2. Hess, S.T., Girirajan, T.P. & Mason, M.D. *Biophys. J.* **91**, 4258–4272 (2006).
3. Betzig, E. *et al. Science* **313**, 1642–1645 (2006).
4. Rust, M.J., Bates, M. & Zhuang, X. *Nat. Methods* **3**, 793–795 (2006).
5. Hess, S.T. *et al. Proc. Natl. Acad. Sci. USA* **104**, 17370–17375 (2007).
6. Shroff, H., Galbraith, C.G., Galbraith, J.A. & Betzig, E. *Nat. Methods* **5**, 417–423 (2008).
7. Huang, B., Wang, W., Bates, M. & Zhuang, X. *Science* **319**, 810–813 (2008).
8. Juette, M.F. *et al. Nat. Methods* **5**, 527–529 (2008).
9. Betzig, E. & Chichester, R.J. *Science* **262**, 1422–1425 (1993).
10. Bartko, A.P. & Dickson, R.M. *J. Phys. Chem. B* **103**, 11237–11241 (1999).
11. Bohmer, M. & Enderlein, J. *J. Opt. Soc. Am. B* **20**, 554–559 (2003).
12. Harms, G.S., Cognet, L., Lommerse, P.H.M., Blab, G.A. & Schmidt, T. *Biophys. J.* **80**, 2396–2408 (2001).
13. Patterson, G.H. & Lippincott-Schwartz, J. *Science* **297**, 1873–1877 (2002).
14. Gurskaya, N.G. *et al. Nat. Biotechnol.* **24**, 461–465 (2006).
15. Fourkas, J.T. *Opt. Lett.* **26**, 211–213 (2001).
16. Lakowicz, J.R. *Principles of Fluorescence Spectroscopy* 3rd ed. (Springer Science, New York, 2006).
17. Weber, G. *J. Opt. Soc. Am.* **46**, 962–970 (1956).
18. Hess, S.T., Sheets, E.D., Wagenknecht-Wiesner, A. & Heikal, A.A. *Biophys. J.* **85**, 2566–2580 (2003).
19. Jacobson, K., Mouritsen, O.G. & Anderson, R.G. *Nat. Cell Biol.* **9**, 7–14 (2007).

nature | methods

Nanoscale imaging of molecular positions and anisotropies

Travis J Gould, Mudalige S Gunewardene, Manasa V Gudheti, Vladislav V Verkhusha, Shu-Rong Yin, Julie A Gosse & Samuel T Hess

Supplementary figures and text:

Supplementary Figure 1

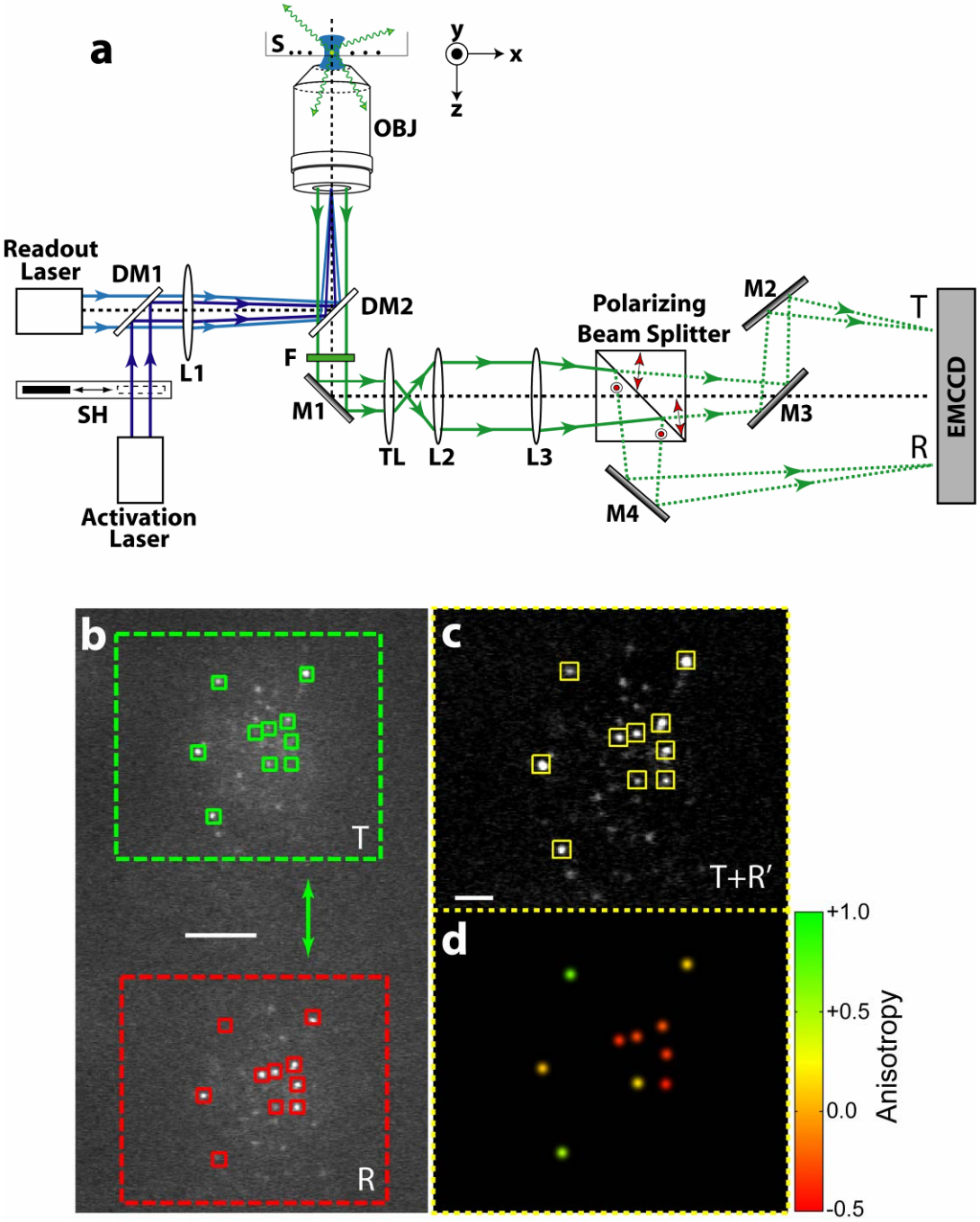

Full experimental setup and sample data acquisition for P-FPALM to determine single molecule anisotropy. (**a**) The activation and readout lasers are combined into a collinear path at dichroic mirror DM1, then focused by L1 to form a waist at the back-aperture of the objective lens (OBJ) after being reflected by dichroic mirror DM2, contained within an inverted microscope (frame not shown). A shutter (SH) controls whether the activation laser illuminates the sample. The sample (S), mounted on the stage of the microscope, is illuminated with an approximately

Gaussian beam profile covering a large area (~300 μm^2) with a waist in the plane of the sample (blue hourglass). The fluorescence photons from the sample (wavy green arrows) are partially collected by the same objective and travel as parallel rays (green lines with green arrows) through DM2, are filtered by emission filter F, reflected by mirror M1, and focused by the microscope tube lens (TL) to form an intermediate image between TL and a second lens L2. The combination of lenses L2 and L3 magnifies the image and focuses it onto the electron multiplying charge coupled device (EMCCD) camera. Before reaching the camera, however, the fluorescence reaches a polarizing beam splitter, which separates the light polarized parallel to its internal interface (red circles, lower path) from the light polarized perpendicular to the internal interface (red arrows, straight through path). Mirrors M2, M3, and M4 are used to adjust the alignment of the two pathways to form separate images of the light from the parallel and perpendicular paths, such that they have the same total path length and the same angle of incidence upon reaching the EMCCD. Lateral coordinates x, and y, and axial coordinate z are shown for reference. Drawing is not to scale. (**b**) A single frame from a polarized FPALM image series of Dendra2-actin expressed in a fixed fibroblast shows the detected emission parallel (the T image) and perpendicular (the R image) to the readout laser (polarization indicated by green arrow) imaged on the same EMCCD chip. After coordinate transformation ($R \rightarrow R'$) to overlap the images, T (dashed green box) and R (dashed red box) are summed, and their sum is used to localize molecules (**c**). Localized molecules in **c** are indicated by small yellow boxes while the small red and green boxes in **b** indicate the relative contributions from each component of polarization. (**d**) Localized molecules are plotted as Gaussian spots (of width much greater than the localization precision for visualization of coloring) and colored (see color bar) according to the anisotropy calculated from Eq.1. Scale bar 5 μm in **b**, 2 μm in **c**.

Supplementary Figure 2

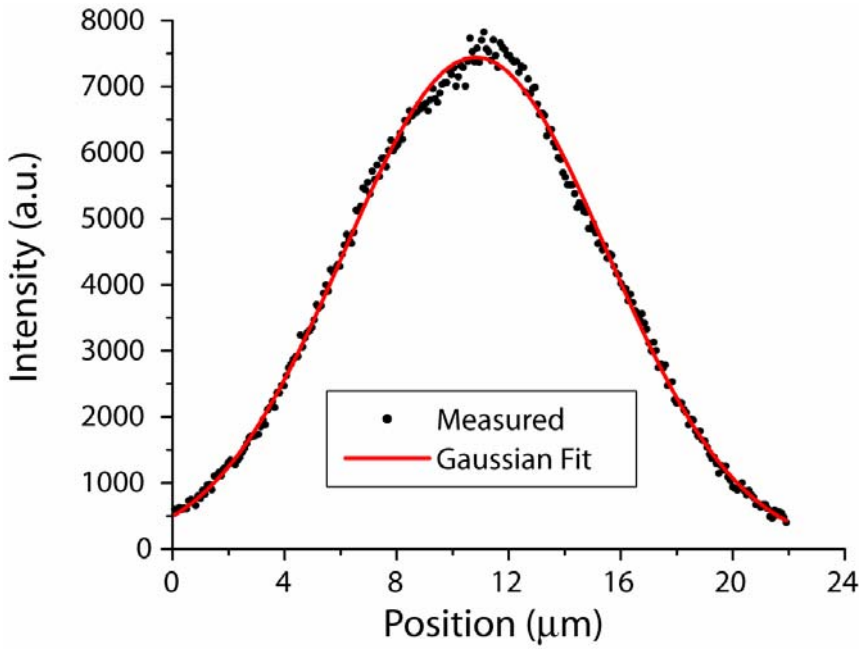

Readout beam illumination profile. The intensity profile of the 556-nm illumination beam was determined from imaging rhodamine B in solution at low excitation intensity (~17 W/cm^2). The detected fluorescence intensity was averaged across the full width of the image of the beam in a strip ~1.7 μm wide, and a linear baseline was subtracted from the profile. The baseline-subtracted measured intensity profile (black points) was then least-squares fitted with a one-dimensional Gaussian (red line).

Supplementary Figure 3

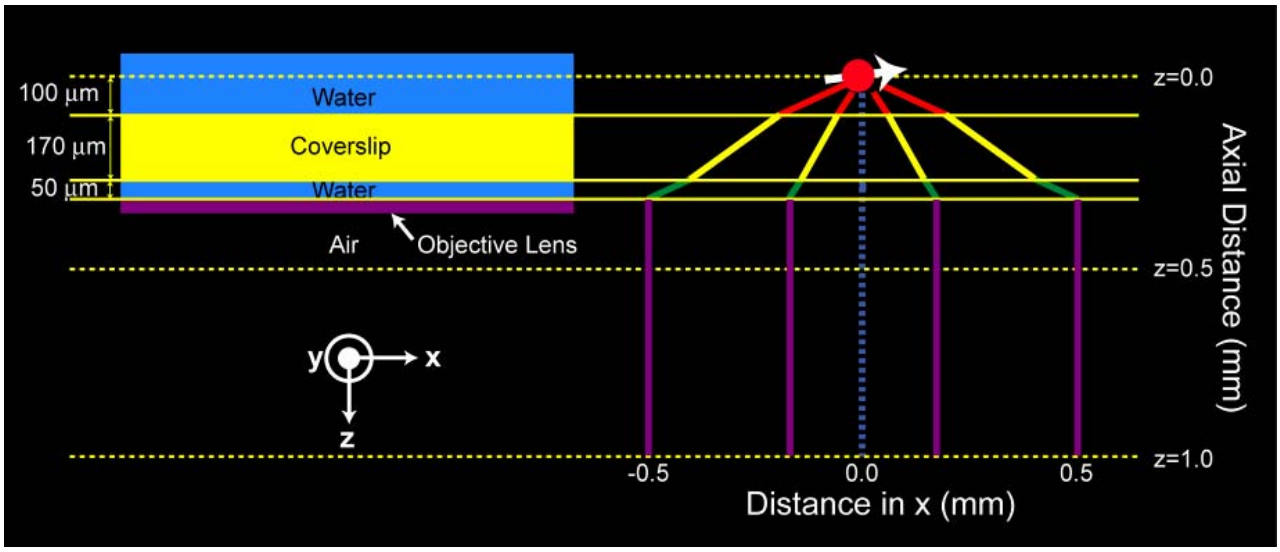

Modeling the fluorescence detected in P-FPALM. A single molecule near the focus of a high-numerical aperture objective (red circle) lens emits dipole radiation according to its transition dipole moment (white arrow). The electric field generated by this dipole is calculated and propagated through the water-coverslip, coverslip-water, and water-objective interfaces (propagation direction shown by red, yellow, green, and purple rays), using the Fresnel equations. The intensity of detected fluorescence in the parallel and perpendicular channels is calculated from the electric field of the light collected by the objective, as a function of dipole position and orientation.

Supplementary Figure 4

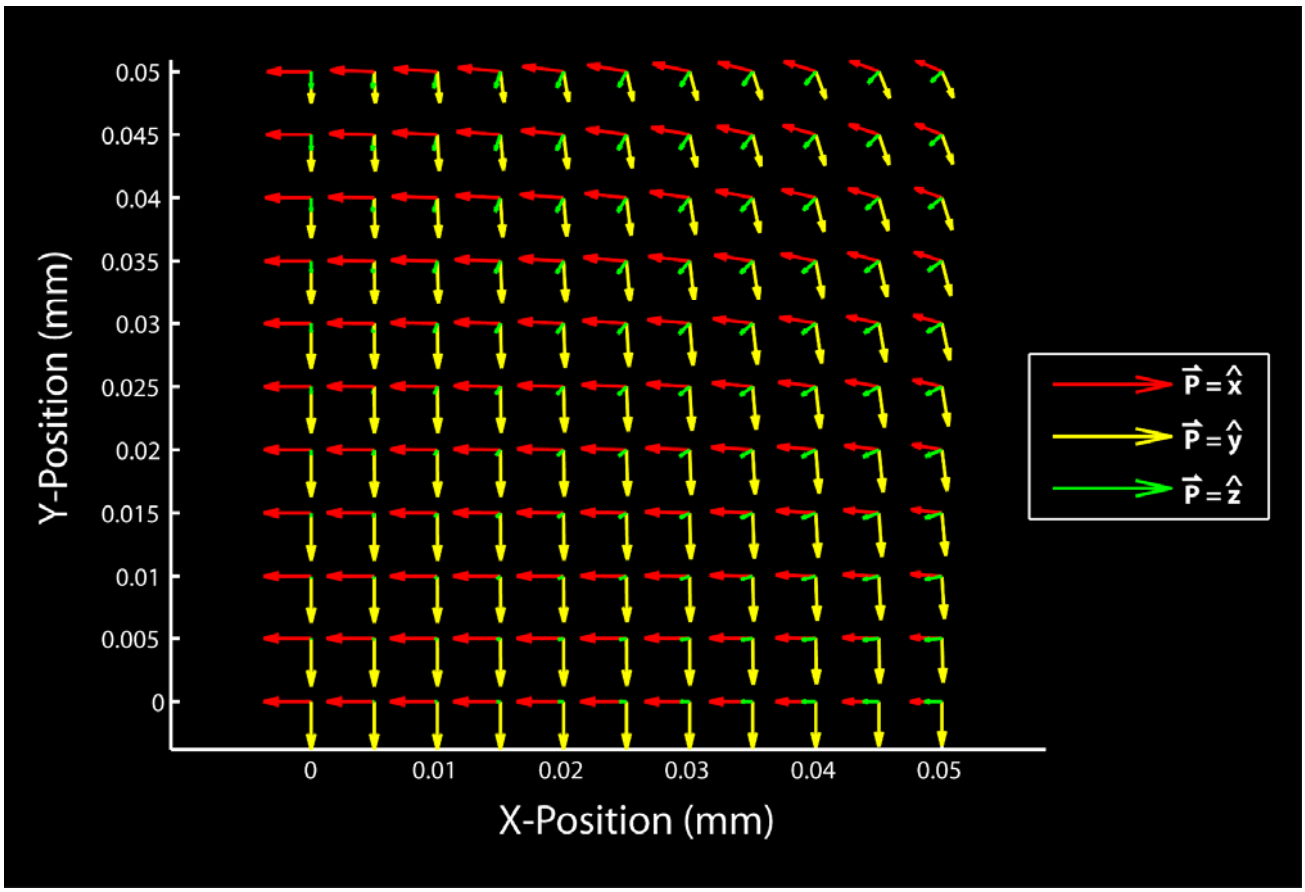

The detected electric field from a dipole near the focus of a 1.2NA water-immersion objective lens. Dipole components oriented along x (red arrows), y (yellow arrows), and z (green arrows) are shown as a function of the position of the dipole in the xy plane. Note that significant tipping of the detected electric field relative to the dipole moment occurs when the dipole is displaced significantly (i.e. >20 μm radially) from the center of the field. In all cases, P-FPALM measurements of anisotropy were made at distances less than 15 μm from the center of the field.

Supplementary Figure 5

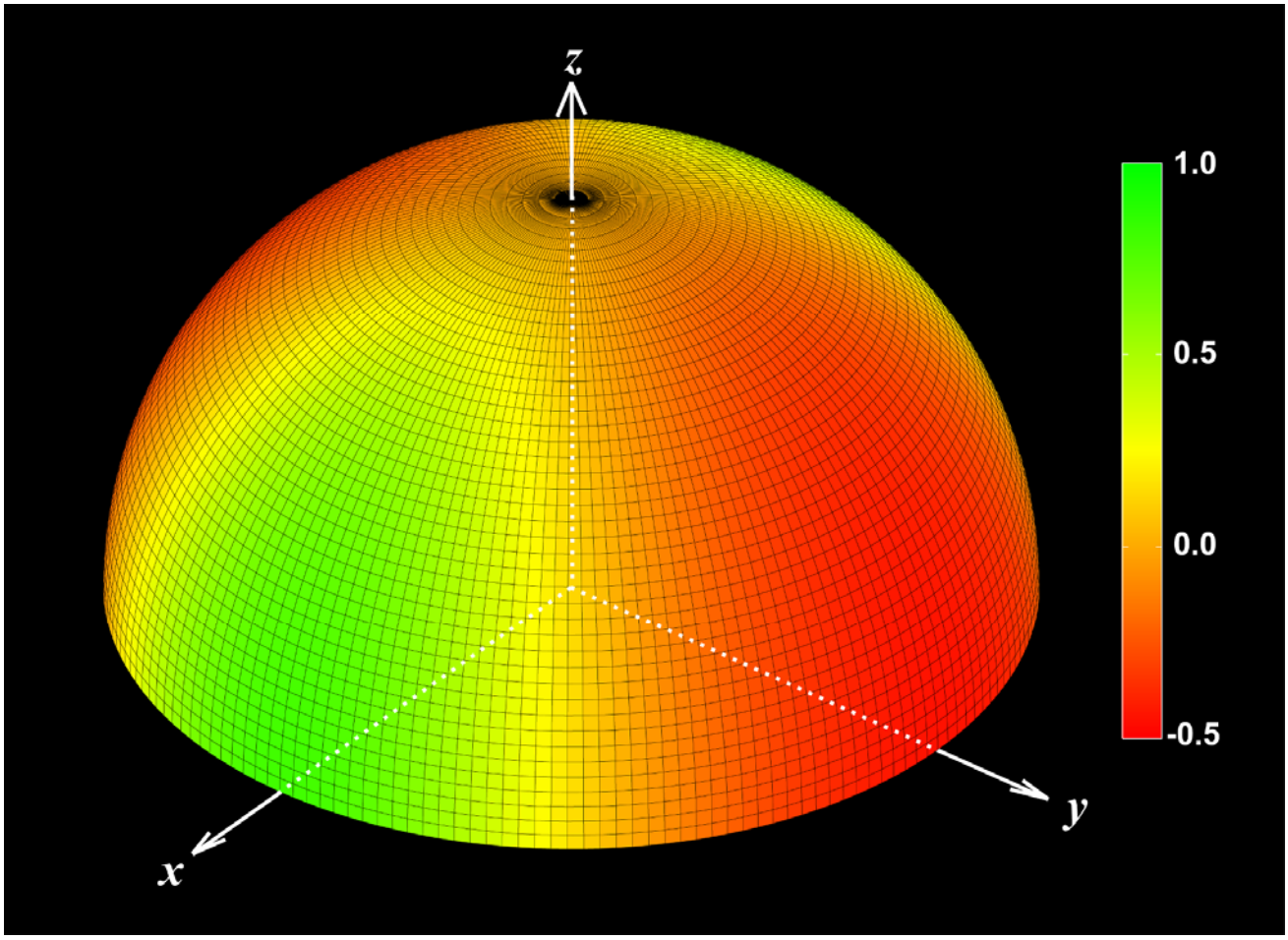

Expected (calculated) detected anisotropy as a function of single-molecule orientation near the center of the field in a P-FPALM microscope. The anisotropy expected for a single molecule (dipole emitter) at the center of the field, in the focal plane of a high-NA objective lens was calculated using Eq. S6 and Eqs. S12, and is shown as a function of probe orientation. Note that the polarization of the laser is along the x-axis. The color on the surface of the sphere indicates the detected anisotropy value (see colorbar) for a molecule with transition dipole moment pointing from the origin to the surface at that point. Note that symmetry dictates the anisotropy values for other orientations not shown (i.e. a molecule with exactly opposite transition dipole moment will have the same expected detected anisotropy).

Supplementary Figure 6

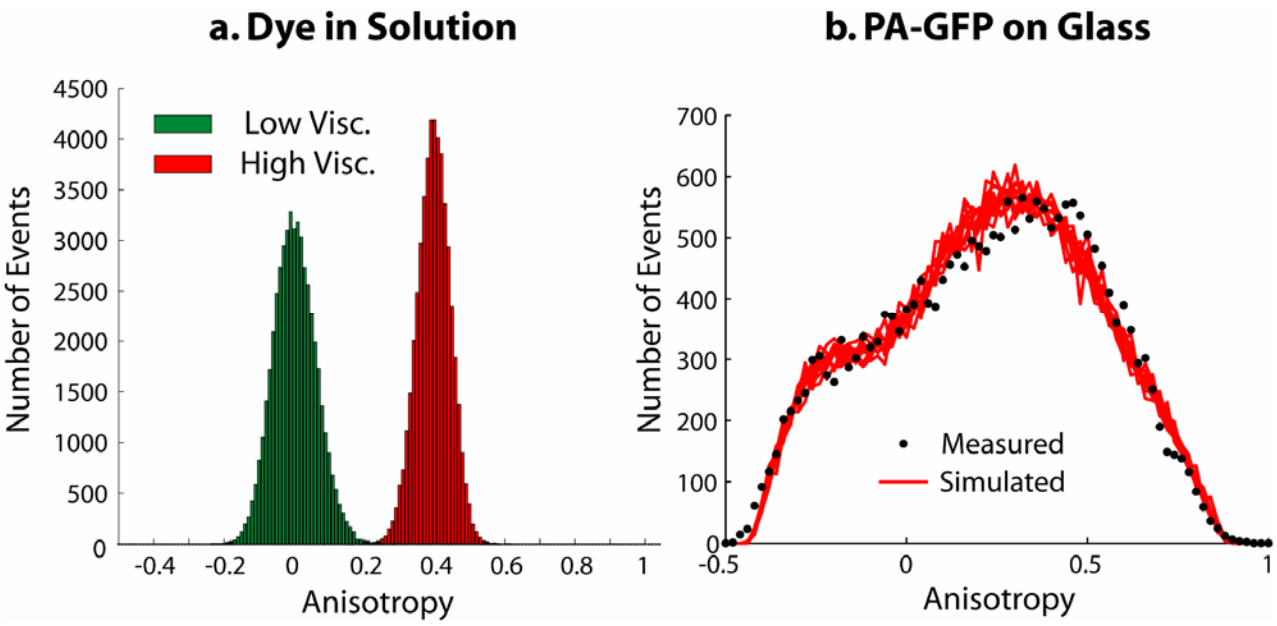

Measured and Monte-Carlo Simulated P-FPALM Anisotropy Histograms. (**a**) Simulated anisotropy histograms for a standard fluorophore with random orientation in solution at low viscosity (Green bars), such that complete randomization of the fluorophore orientation occurs before emission. (Red bars) At high viscosity, the fluorophore does not reorient, and emits as a dipole moment parallel to the transition dipole moment. Simulations include the effect of rotation of the electric field by the objective lens (see Suppl. Fig. 4). The mean anisotropies of 0.0016 and 0.4002 for low and high viscosity, respectively, are in good agreement with predictions from theory in low-NA systems, and with measurements made on rhodamine B in solution (see Supplementary Methods). (**b**) Measured anisotropy histogram for PA-GFP immobilized on glass (black circles) is described by simulations (red lines showing ten independent simulation runs) using two populations of photoactivatable molecules with non-random orientation.

Supplementary Figure 7

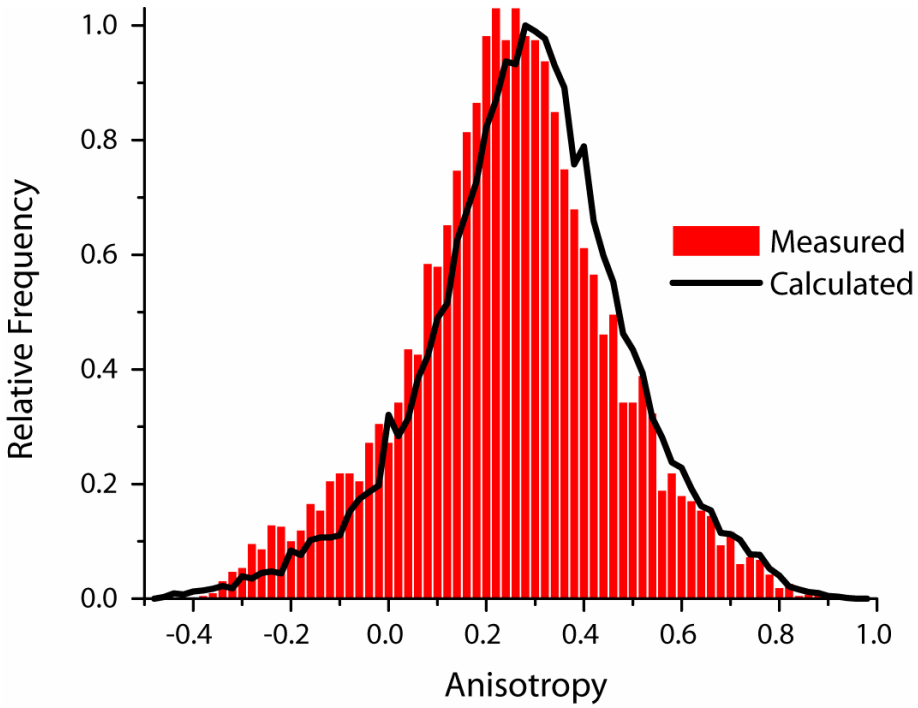

Measured anisotropy histogram for caged fluorescein in agarose gel (red bars) compared with anisotropy histogram expected (calculated) from theory (black line). Results show data for 9,712 measured and 49,887 calculated molecules, respectively.

Supplementary Figure 8

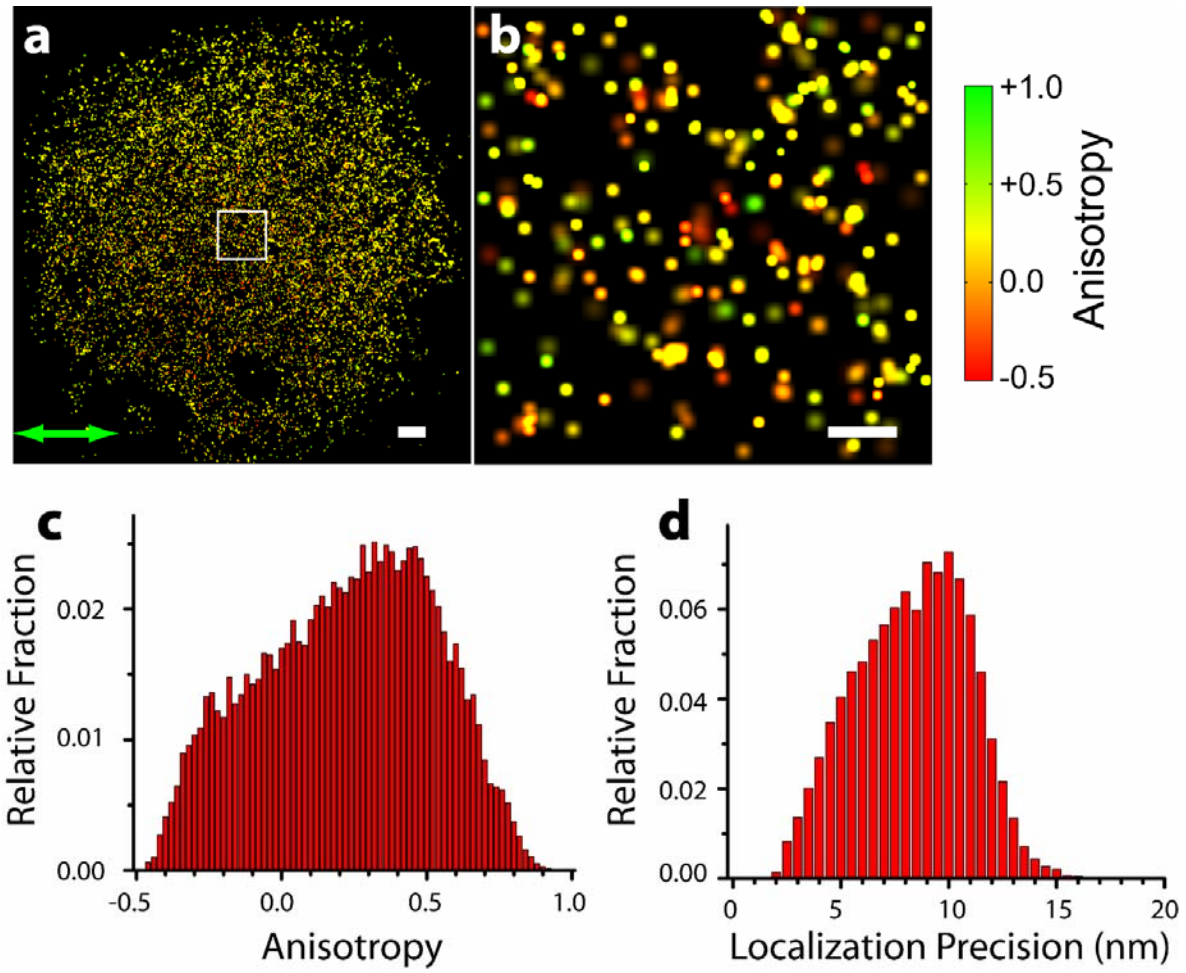

P-FPALM image of PA-GFP on coverglass. (**a**) P-FPALM image of PA-GFP dried on a glass coverslip (22,452 localized molecules). Note that the most frequent value for r is not zero because the PA-GFP molecules are presumably immobilized on the surface. The spatial dependence of the anisotropy for the PA-GFP on glass is weak, demonstrating that the differences observed in images of Dendra2-actin in cells are significant. Scale bar 1 μm. The green arrow indicates direction of polarization for readout beam (488 nm). (**b**) Zoom-in of boxed region in **a** (310 molecules). Scale bar 250 nm. Color bar indicates anisotropy for **a** and **b**. (**c**) Distribution of single molecule anisotropies of molecules shown in **a**. (**d**) Distribution of localization precision of single molecules in **a** as calculated by Eq. S1.

Supplementary Figure 9

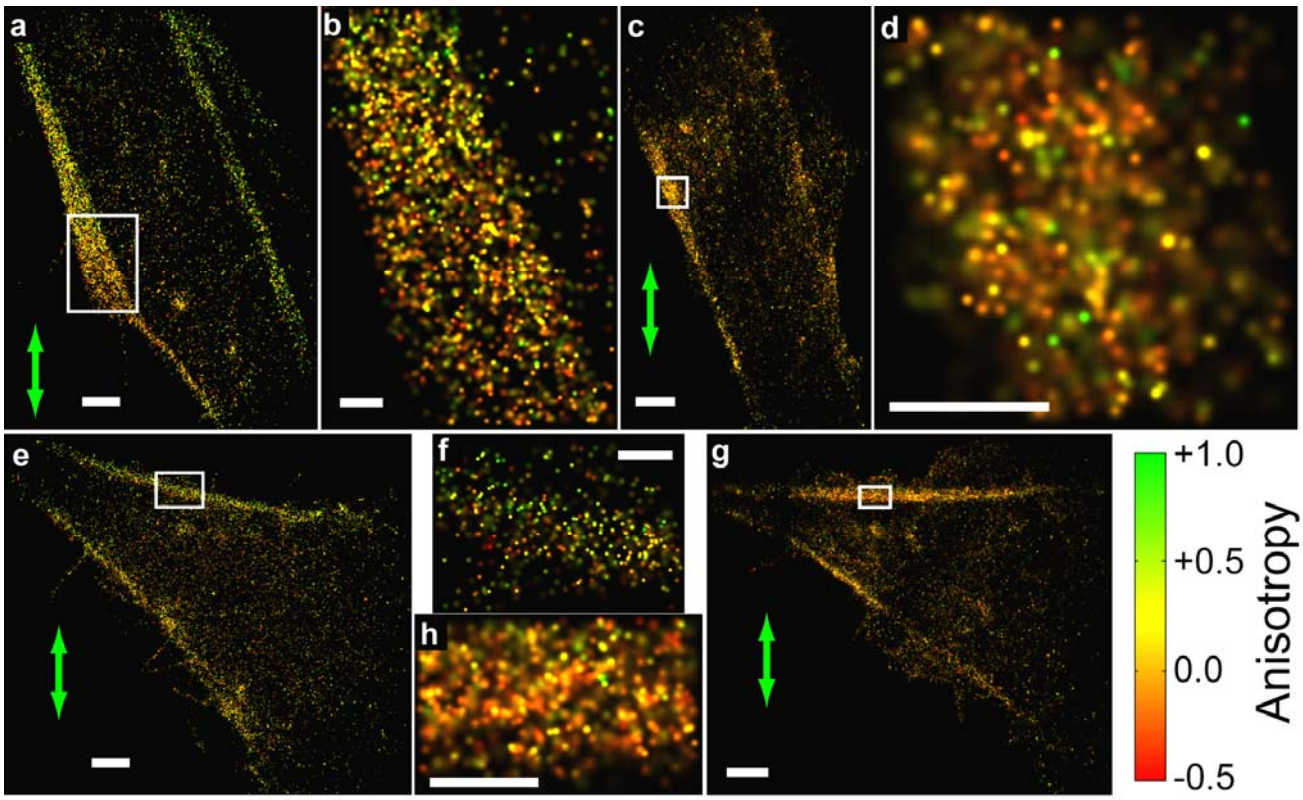

Additional P-FPALM images of Dendra2-actin expressed in fixed fibroblasts. Note the presence of filamentous structures of actin that show clear trends in single molecule anisotropy. (**a**) 11,244 localized molecules. (**b**) Zoom-in of boxed region in **a**: 2,287 localized molecules. (**c**) 25,998 localized molecules. (**d**) Zoom-in of boxed region in **c**: 1,198 localized molecules. (**e**) 15,593 localized molecules. (**f**) Zoom-in of boxed region in **e**: 642 localized molecules. (**g**) 36,002 localized molecules. (**h**) Zoom-in of boxed region in **g**: 1,136 localized molecules. Green arrows indicate polarization of read-out laser (556 nm). Scale bar is 1 μm for **a**, **c**, **e**, and **g**. Scale bar is 250 nm for **b**, **d**, **f**, and **h**. Color bar indicates anisotropy for **a** - **h**. Brightness and contrast were adjusted linearly in **a** - **g** for display.

Supplementary Figure 10

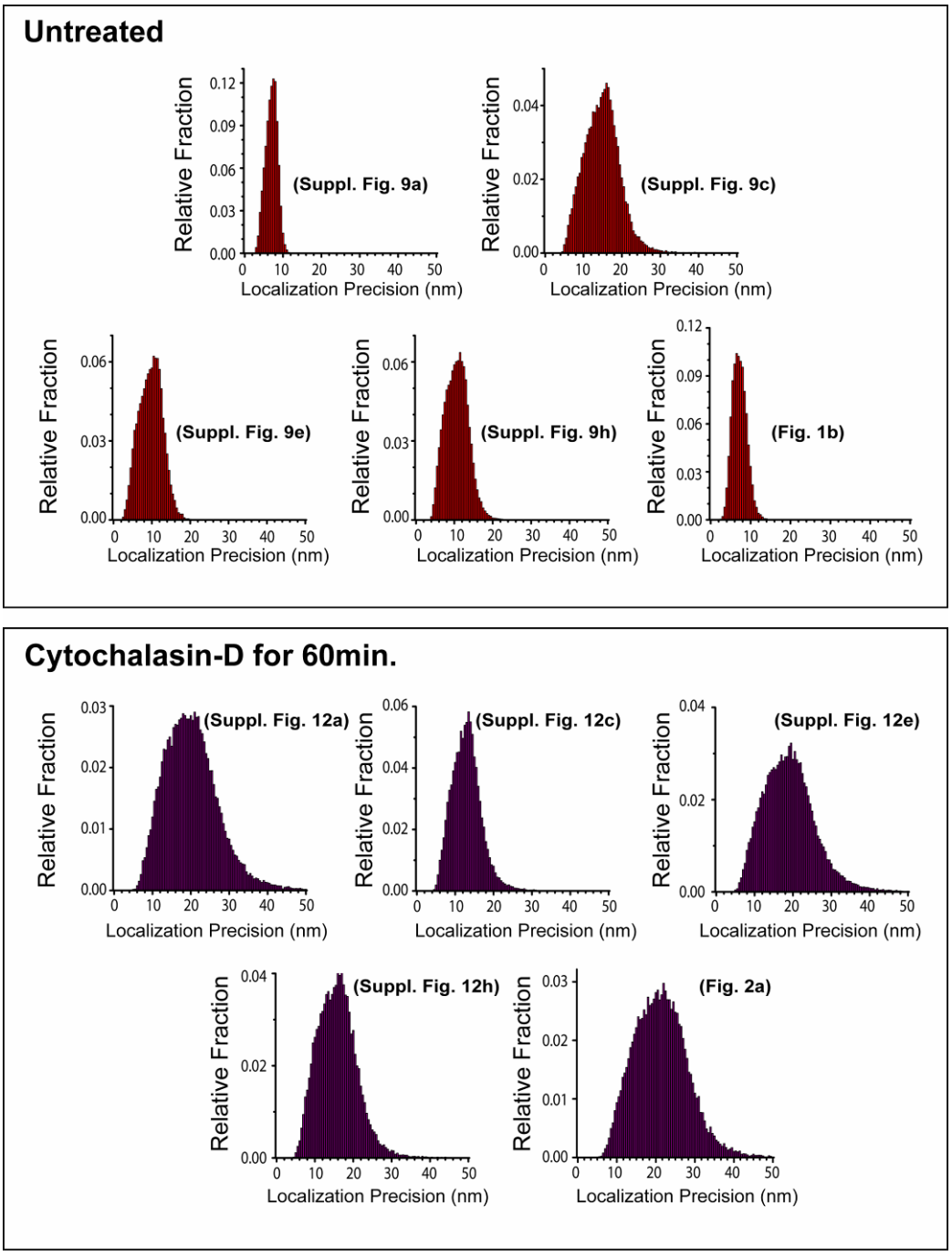

Histograms of calculated localization precision. Localization precision was calculated using Eq. S1 for selected P-FPALM images of untreated fibroblasts (top) and fibroblasts treated with cytochalasin D for 60 min (bottom). Data shown includes all cells shown in Dendra2-actin images within the text and supplementary material.

Supplementary Figure 11

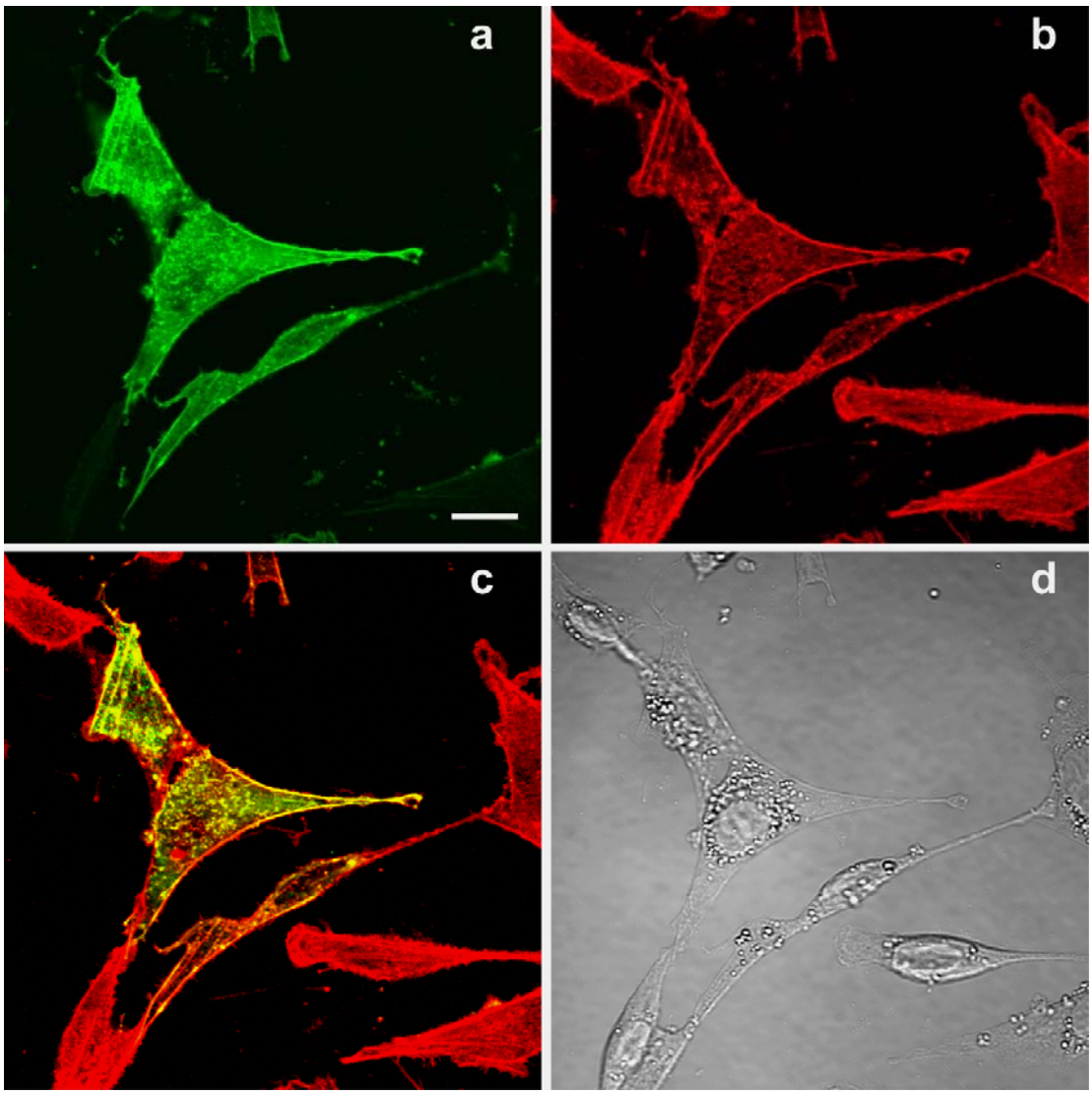

Confocal image of Dendra2-actin transfected fibroblasts which were fixed, permeabilized, and stained with Alexa-680-phalloidin. (**a**) and (**b**) show the pattern of labeling obtained for Dendra2-actin and Alexa-680-phalloidin respectively, demonstrating colocalization of the two markers for actin within the cell. (**c**) Overlay of **a** and **b**. Since phalloidin labels a higher fraction of cells than were transfected, we observe cells with Alexa- 680-phalloidin staining that are not labeled with Dendra2-actin. (**d**) Transmitted light image of the same region. Scale bar of 10 μm in **a** applies to all panels. Brightness and contrast were adjusted linearly in **a** - **d** for display.

Supplementary Figure 12

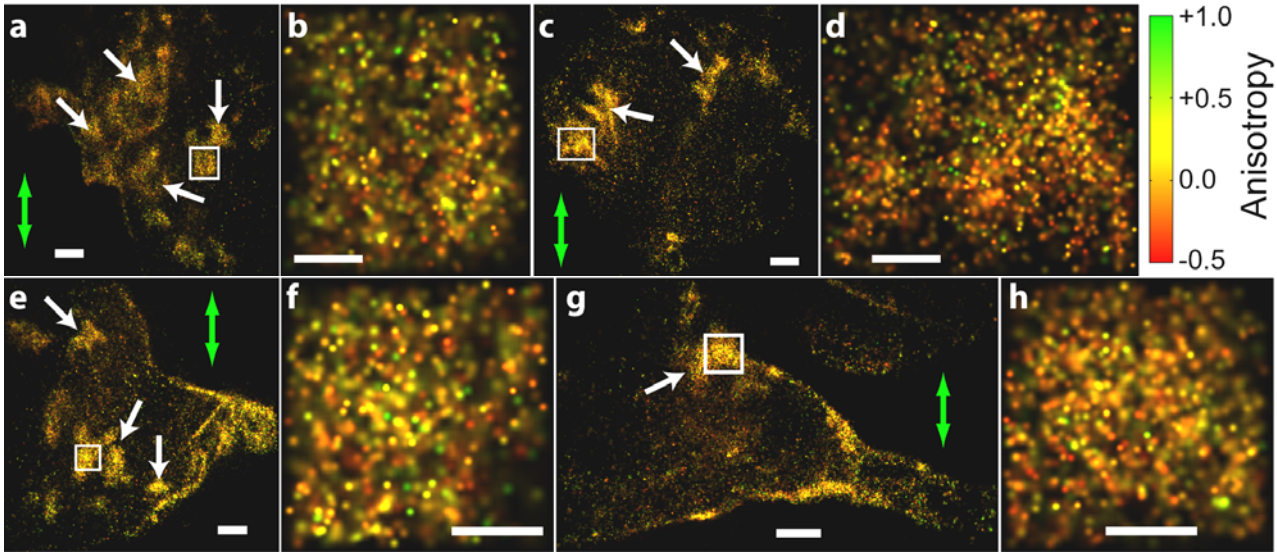

Additional P-FPALM images of Dendra2-actin expressed in fixed fibroblasts incubated in 1 μM cytochalasin D for 60 min before fixation. (**a**) 49,916 localized molecules. (**b**) Zoom-in of boxed region in **a**: 2,334 localized molecules. (**c**) 30,515 localized molecules. (**d**) Zoom-in of boxed region in **c**: 2,794 localized molecules. (**e**) 45,095 localized molecules. (**f**) Zoom-in of boxed region in **e**: 1,612 localized molecules. (**g**) 26,491 localized molecules. (**h**) Zoom-in of boxed region in **g**: 1,794 localized molecules. Green arrows indicate polarization of read-out laser (556 nm). White arrows indicate globular clusters with molecules emitting parallel and perpendicular to the excitation. Scale bar is 1 μm for **a**, **c**, **e**, and **g**; scale bar is 250 nm for **b**, **d**, **f**, and **h**. Color bar indicates anisotropy for **a-h**. Brightness and contrast were adjusted linearly in **a** - **h** for display.

Supplementary Figure 13

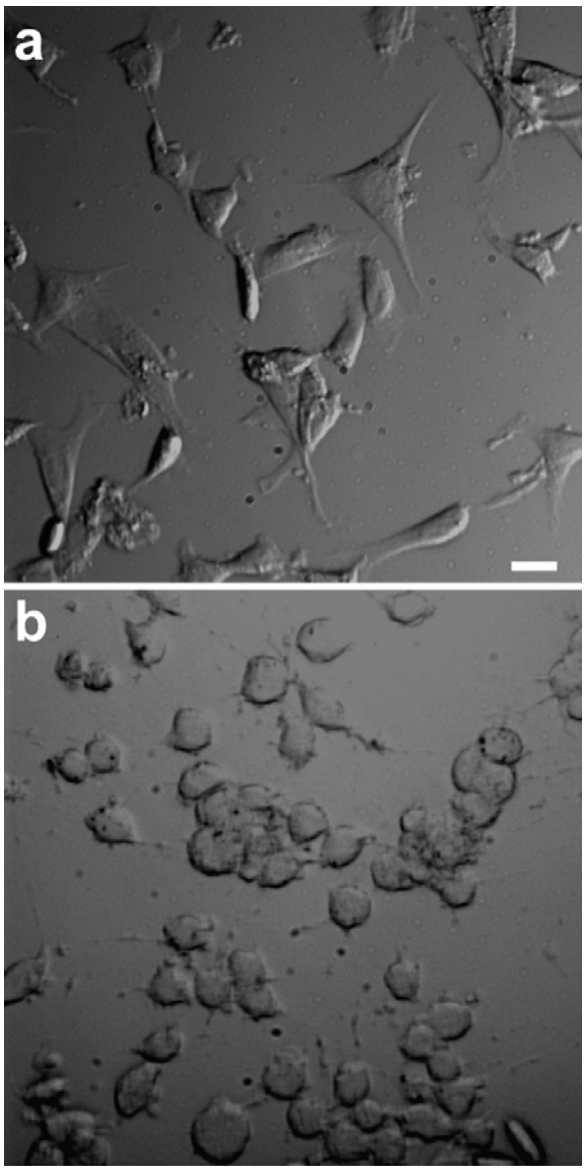

Transmitted light images of fixed fibroblasts. Images were obtained under low magnification for (**a**) fixed fibroblasts and (**b**) fibroblasts treated with cytochalasin D for 60 min before fixation and demonstrate differences in morphologies between untreated and treated cells. Scale bar of 20 μm in **a** applies to both panels. Brightness and contrast were adjusted linearly in **a** and **b** for display.

Supplementary Figure 14

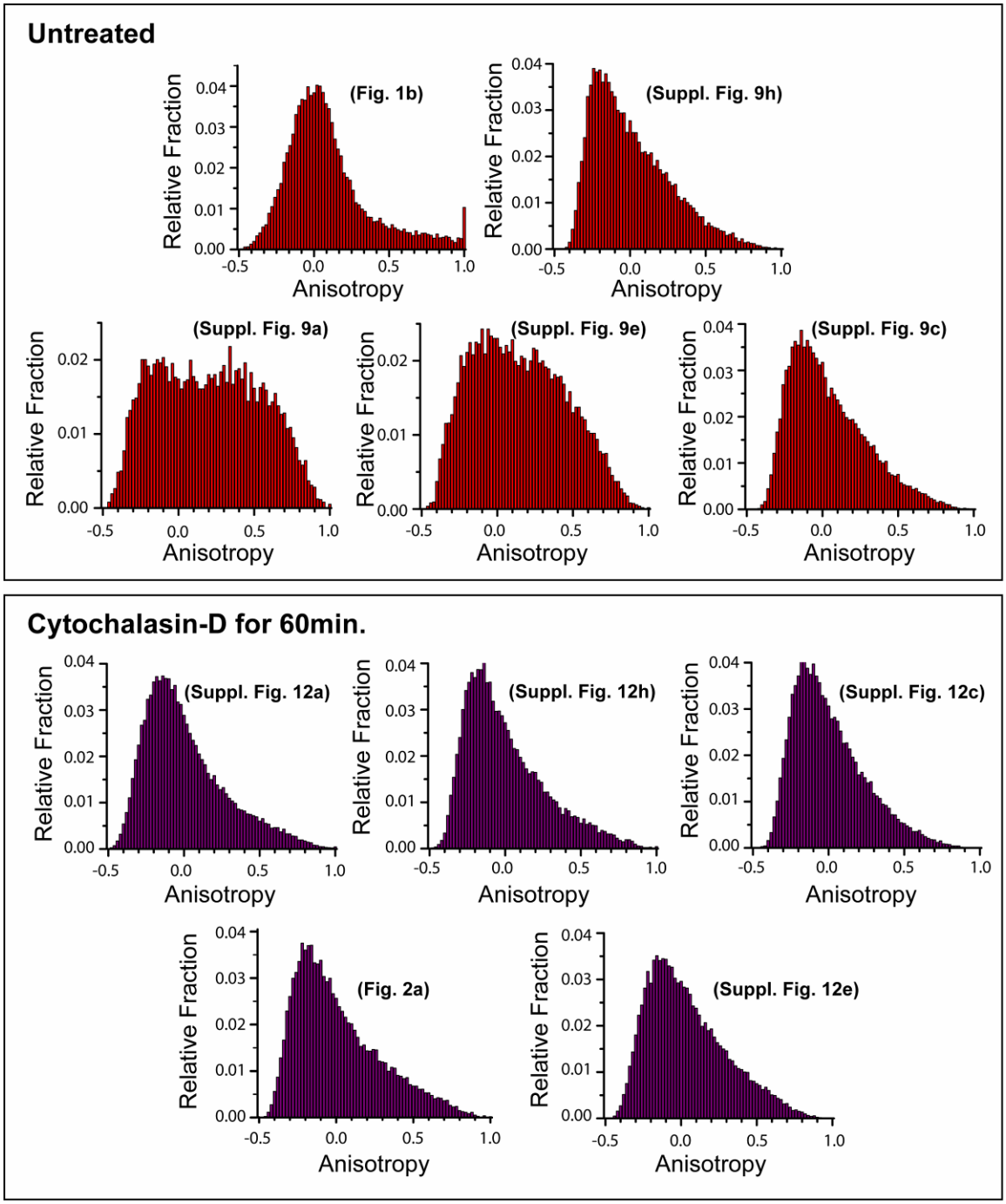

Histograms of anisotropy for selected P-FPALM images of untreated fibroblasts (top, total n=30) and fibroblasts treated with cytochalasin D for 60 min (bottom). All molecules localized in the given cell are included in each histogram. Corresponding cell images are shown in parentheses.

Supplementary Figure 15

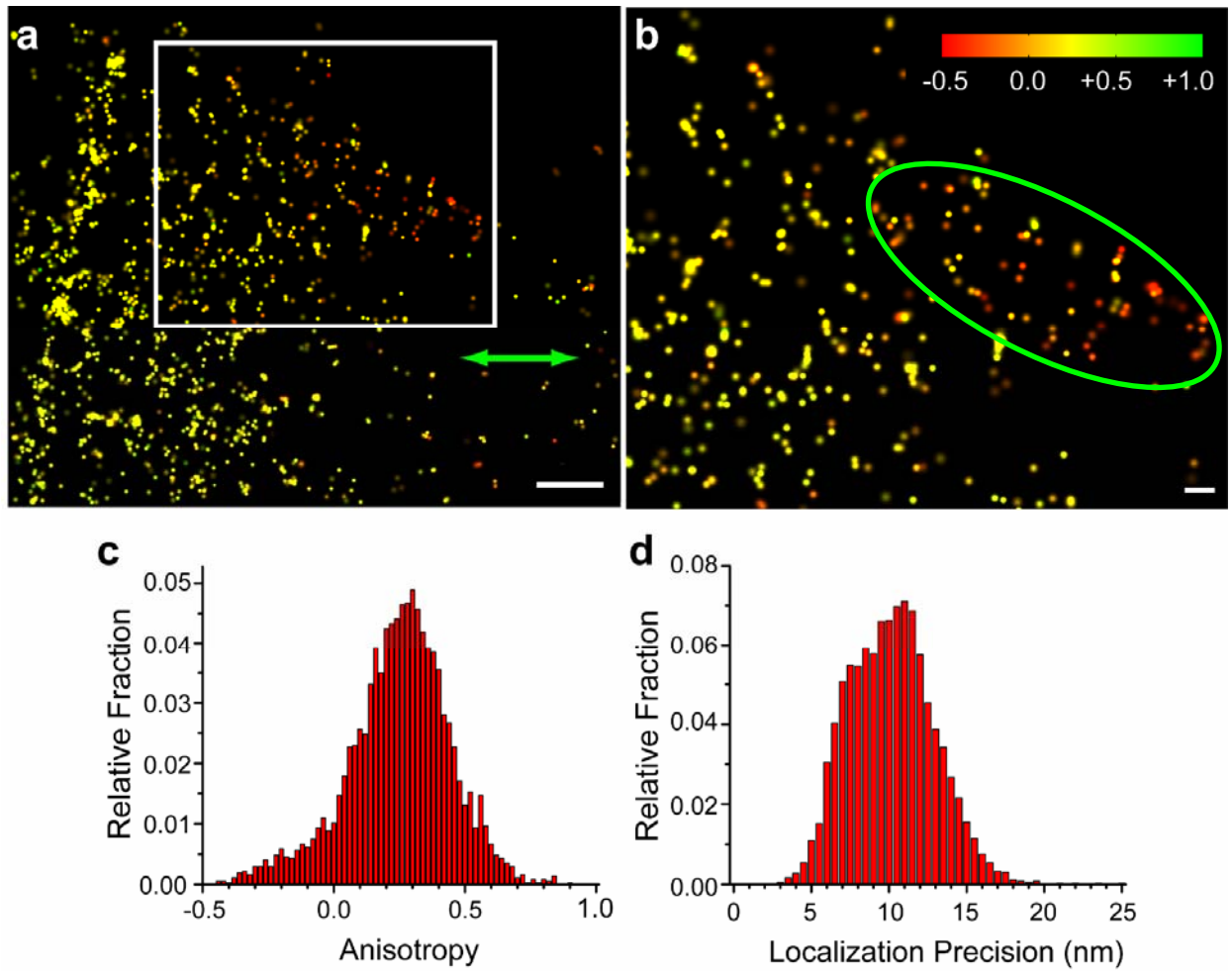

P-FPALM imaging of PAGFP-HA. (**a**) P-FPALM image of PAGFP-HA expressed in a fixed fibroblast (1,601 molecules). Scale bar 1 μm. The green arrow indicates the direction of polarization for the readout beam (496 nm). (**b**) Zoom-in of boxed region in **a** (412 molecules). Scale bar 250 nm. Color bar indicates anisotropy for **a** and **b**. Green ellipse indicates cluster of molecules with similar (small or negative) anisotropy values. (**c**) Distribution of single molecule anisotropies for all molecules localized in the cell shown in **a**. (**d**) Distribution of localization precision for all molecules localized in the cell shown in **a** as calculated by Eq. S1.

Supplementary Figure 16.

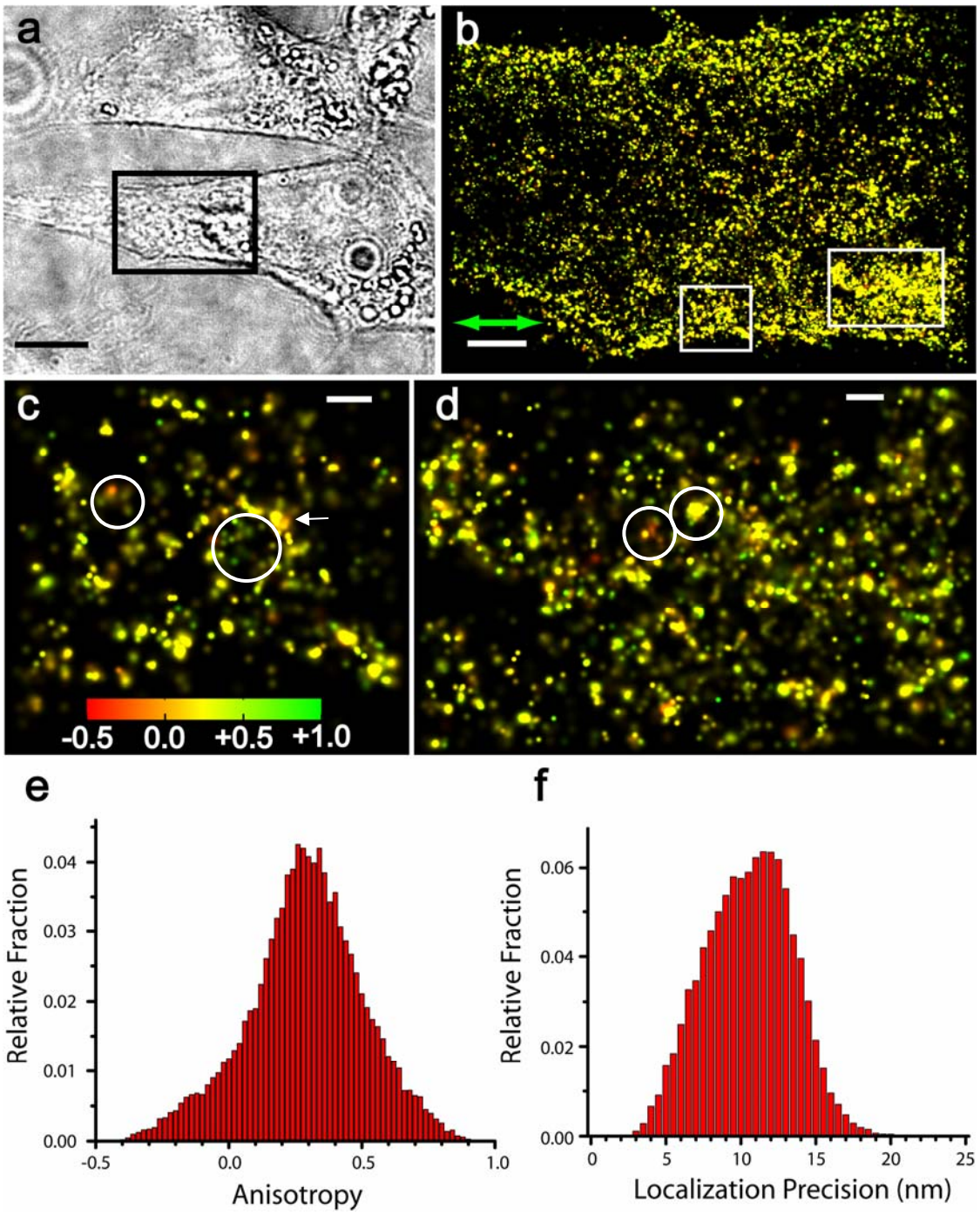

P-FPALM image of Dendra2-HA expressed in a fixed fibroblast. (**a**) Transmitted light image. Scale bar 10 μm. (**b**) P-FPALM image (30,088 molecules) of boxed region in **a**. Scale bar 2 μm. The green arrow indicates the direction of polarization for the readout beam (556 nm). (**c**) (1,202 molecules) and (**d**) (4,067 molecules) show zoom-ins of boxed regions in **b**. Scale bar 250 nm. Color bar indicates anisotropy for **b,c** and **d**. Circles and arrow in **c** and **d** indicate small clusters with anisotropy values different from neighboring clusters. (**e**) Distribution of single molecule anisotropies for molecules localized in **b**. (**f**) Distribution of localization precision for molecules localized in **b**, as calculated by Eq. S1.

Supplementary Figure 17

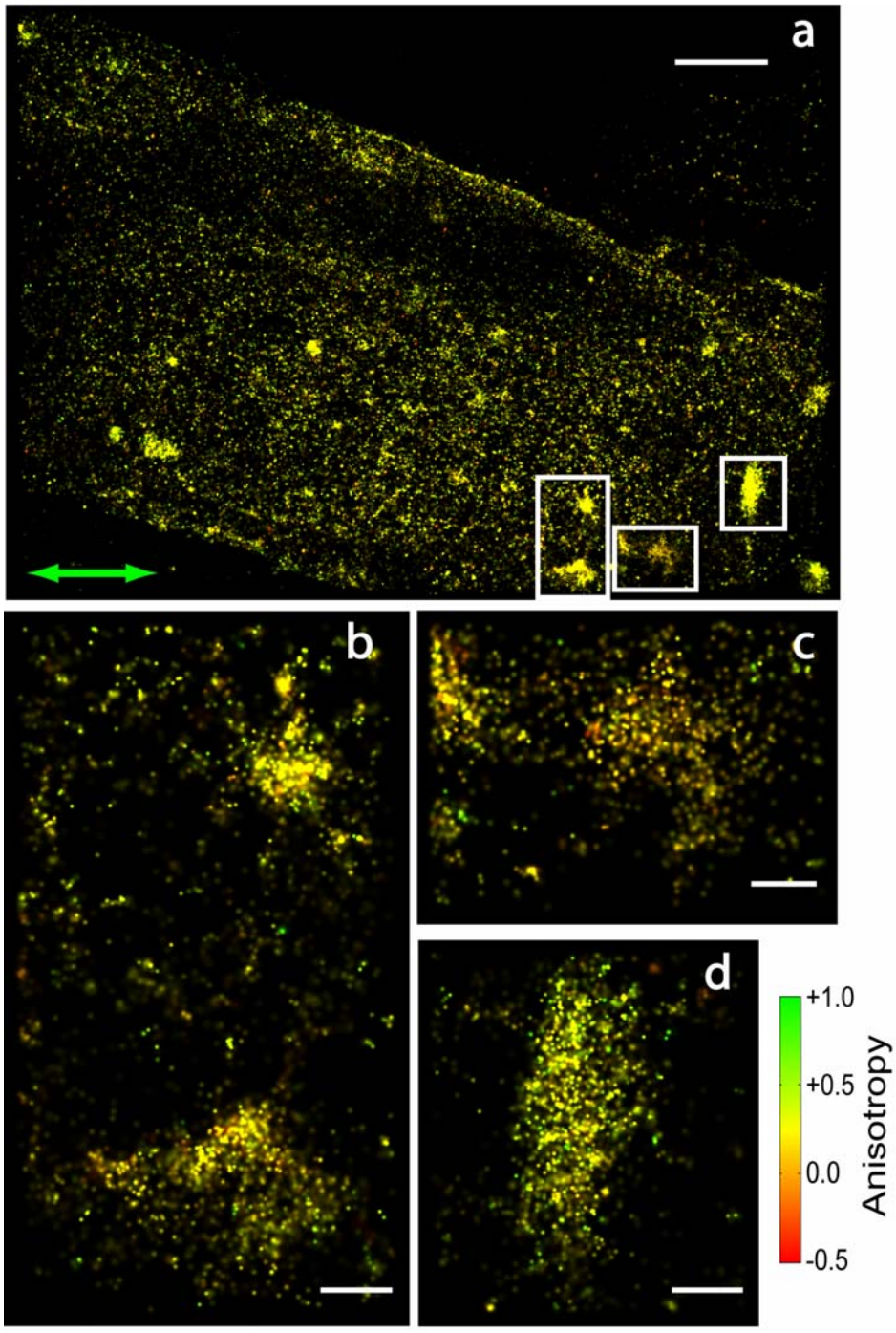

P-FPALM image of Dendra2-HA expressed in a fixed fibroblast. (**a**) P-FPALM image (85,977 molecules) , Scale bar 2 μm. The green arrow indicates the direction of polarization for the readout beam (556 nm). (**b**) (4,346 molecules), (**c**) (1,504 molecules) and (**d**) (2,460 molecules) show zoom-ins of boxed regions in **a**. Scale bar 250 nm. Color bar indicates anisotropy. Note the differences in anisotropy value from cluster to cluster, and in some cases within clusters.

Supplementary Table 1. Filter Combinations Used for Fluorescence Detection

Fluorophore	Dichroic (DM2)	Emission Filter (F)
Dendra2	T565LP*	ET605/70M*
PAGFP	Z488RDC*	HQ535/50M*

*Chroma Technology, Rockingham, VT

Supplementary Table 2. Acquisition and Rendering Parameters

Fig.	CD Treat.	Number of Frames	Power Readout (mW)	Power @ 405 nm (μW)	405 ON (Frames)	Frame Rate (Hz)	Number Molecules Localized	Acquisition Time (s)	Acquisition Time (min)	Bkgd. Noise (Phot./pix.)
1b	None	4900	24.6*	12.8	all	31.2	21,525	156.9	2.62	7.0
2a	60 min	8000	8.5*	0.147	5000-8000	31.2	32,553	256.2	4.27	8.1
S. 9a	None	4900	24.6*	--	none	31.2	11,244	156.9	2.62	6.0
S. 9c	None	8000	8.5*	0.147	all	31.2	25,998	256.2	4.27	5.1
S. 9e	None	2500	24.6*	--	none	31.2	15,593	80.1	1.33	7.4
S. 9h	None	8000	8.5*	0.147	all	31.2	36,002	256.2	4.27	3.5
S. 12a	60 min	8000	8.5*	0.147	5000-8000	31.2	49,916	256.2	4.27	7.3
S. 12c	60 min	8000	8.5*	0.147	all	31.2	30,515	256.2	4.27	4.1
S. 12e	60 min	8000	8.5*	0.147	5000-8000	31.2	45,095	256.2	4.27	6.7
S. 12g	60 min	8000	8.5*	0.147	4000-8000	31.2	26,491	256.2	4.27	5.6
S. 15a	N/A	445	5.7†	-	none	19.3	3,744	23.0	0.38	5.1
S. 16	N/A	10000	12.85*	‡	720-7000‡	31.2	30,582	320.5	5.34	2.9
S. 17	N/A	17500	12.85*	$	1400-17500$	31.2	85,977	560.9	9.35	3.0

* 556nm laser. †496nm laser. Powers measured at sample.
‡ Frames 720 – 1,600: 0.3 μW, 1,600-3,000: 0.90 μW, 3,000-5,200: 3.0 μW, 5,200-7,000: 9.0 μW, 7,000-10,000: 30 μW.
$ Frames 1,400 – 7,000: 0.3 μW, 7,000-9,000: 0.90 μW, 9,000-12,500: 3.0 μW, 12,500-15,000: 9.0 μW, 15,000-17,500: 30 μW.

Supplementary Methods

Sample Preparation

A. Photoactivatable Green Fluorescent Protein on Glass. Solutions of 4 μM photoactivatable green fluorescent protein (PAGFP)[1] were made by diluting the initial stock (kindly provided by Dr. G.H. Patterson, National Institute of Child Health and Human Development) in UV-treated (see below for UV-treatment protocol) HPLC grade water (Sigma-Aldrich, MO) and a ~0.5 μl droplet was placed and spread on a #1.5 glass coverslip (Corning Life Sciences, NY) and allowed to evaporate slowly.

B. Dendra2-Actin Construct. A humanized version of the Dendra2 gene from pDendra2-C vector (Evrogen, Moscow, Russia) was swapped with the EGFP sequence in pEGFP-actin plasmid (Clontech, CA) resulting in the pDendra2-actin plasmid encoding the Dendra2-actin fusion protein. For production, plasmids were transformed into chemically competent DH5α bacterial host. The plasmid minipreps were obtained using QIAprep Spin kit (Qiagen, MD) after overnight culture.

C. Dendra2-HA Construct. This plasmid was constructed using a pEGFP-N1 vector where HA-x31 open reading frame (ORF) was inserted between Pst I and Xma I sites. The 9th nucleotide C of the Dendra2 ORF was silently mutated to A to eliminate the Xma I site so that the Dendra2 ORF was inserted between Xma I and Not I sites, replacing EGFP from the vector.

D. Cell Culture. HAb2 fibroblasts were grown to ~80% confluence in eight-well chambers with #1.5 coverslip bottom (Labtek II, Nalge-Nunc International Corp.) in Dulbecco's modified eagle's medium (Gibco/Invitrogen, CA) supplemented with 10% calf bovine serum (ATCC, VA) without phenol red or antibiotics. Cells were transfected with ~1 μg per well of pDendra2-actin, pDendra2-HA, or PAGFP-HA[2] using Lipofectamine 2000 (Invitrogen) in Opti-MEM reduced-

serum media (Gibco/Invitrogen) without antibiotics according to the manufacturer's directions and then grown for an additional 24–30 h. For fixation, cells were removed from the incubator, rinsed three times in UV-bleached PBS (see below), incubated for ~30 min in 4% paraformaldehyde (Sigma–Aldrich) in PBS at room temperature, and rinsed three more times with UV-bleached PBS. To disrupt the actin cytoskeleton, cells were incubated with 1 μM cytochalasin-D (C2618, Sigma-Aldrich) at 37° C for 60 min before fixation. The cytochalasin D stock (5 mg/ml in DMSO) was dissolved in PBS at room temperature.

E. Sample for Correlation of R (Reflected) and T (Transmitted) Images. A 1.0 μl droplet of ~100 nM, 100 nm fluorescent beads (FluoSpheres, Molecular Probes/Invitrogen, Carlsbad, CA) was placed on a #1.5 glass coverslip (Corning Life Sciences, Corning, NY) and allowed to evaporate slowly.

F. Low-Background Water. To reduce background signal from fluorescent contaminants in the buffer, cells were imaged in UV-bleached PBS. Approximately 50 mL of PBS in a 200 mL glass beaker was exposed to the light from a 100 W UV lamp for ~15 min. The same procedure was used to reduce background fluorescence from high purity liquid chromatography (HPLC) grade water (Sigma-Aldrich) used as immersion liquid.

Experimental Setup

The full experimental setup, shown in Suppl. Fig. 1, consists of a standard FPALM geometry[2,3] with a modified detection path inspired by the detection path used in BP-FPALM.[4] Samples labeled with Dendra2-actin and Dendra2-HA, PAGFP, or PAGFP-HA were read out using a 556 nm diode laser (LRS-556-NM-100-10, Laserglow.com limited, Toronto, Canada), the 488 nm line of an Ar+ laser (532-A-A03, Omnichrome, Chino, CA), or the 496 nm line of an

Ar+ laser (10 W Innova 310, Coherent, Santa Clara, CA), respectively. A 405 nm diode laser (BCL-405-15, low noise model, Crystalaser, Reno, NV) was used for activation of PAFPs. The readout and activation lasers were combined using a dichroic mirror (Z405RDC, Chroma Technology, Rockingham, VT) and focused at the back aperture of the 60X 1.2 numerical aperture (NA) water-immersion objective lens (UPLAPO60XW, Olympus) by a lens (f=+300 mm) (Newport Corporation, Irvine, CA) located near the back port of the inverted microscope (IX71, Olympus America, Melville, NY). Illumination by the Ar+ laser could be turned on and off using a software-controlled, motorized filter wheel (Thorlabs, Newton, New Jersey). An electronic shutter (SH05, TSC001 Thorlabs, Newton, New Jersey) was used to control illumination by the activation laser. Fluorescence from the sample was collected by the same objective, separated from the laser light by a second dichroic mirror, band-pass filtered (see Suppl. Table 1 for filter combinations), and focused to an intermediate focal plane by the microscope tube lens. Two additional lenses (f=+60 mm and f=+200 mm) (Newport Corporation, Irvine, CA) imaged the intermediate focal plane onto the EMCCD camera (iXon+ DU897DCS-BV, Andor Technology, South Windsor, CT). A polarizing beam splitter (10FC16PB.3, Newport Corporation, Irvine, CA) placed in the detection path in front of the camera separated the detected fluorescence into components polarized parallel and perpendicular to the internal interface of the beam splitter. Additional mirrors (adjusted to equate the total path length from tube lens to camera for both detection paths) directed each detection path to spatially separated locations on the same camera.

The peak intensities at the center of the laser illumination profiles were: 4,700-17,100 W/cm^2 for the 556 nm laser, ~11,000 W/cm^2 for the 488 nm laser and ~2,960 W/cm^2 for the 496nm laser. The 1/e^2 radii of the profiles were: 9.1-10.4 μm for the 556 nm beam, 11.2-11.8

μm for the 488 nm beam and 10.2 -11.2 μm for the 496nm beam. A typical beam profile fitted to a Gaussian is shown in Suppl. Fig. 2.

Image Acquisition

Samples labeled with either PAGFP, PAGFP-HA, Dendra2-actin, or Dendra2-HA were imaged at 9.9 Hz (EM gain 300), 19.3 Hz (EM gain 200), 30.1 Hz (EM gain 200), and 30.1 Hz (EM gain 200), respectively (see Suppl. Table 2). On each day of experiment, 100 nm fluorescent beads dried on a coverslip were imaged to enable correlation of the two detection ROIs (in principle, this calibration is only required at the beginning of experiments, and whenever adjustments have been made to the detection path). All images were saved in TIF format. Laser beam image profiles of 488nm and 496nm lasers were captured by illuminating an aqueous FITC solution, while an aqueous solution of Rhodamine B (RB; Sigma-Aldrich) was used for the 556nm laser.

Measurement of Relative Transmission Efficiencies of Polarizations (G-Factor)

A ~632 nm laser mounted with a polarizer directly in front of the exit aperture was used to generate a beam with either parallel or perpendicular polarization. The mirrors M2, M3, M4 and the polarizing beam splitter (BS; see Suppl. Fig. 1a) were separately placed in front of the polarized 632 nm laser and the incident, reflected, and transmitted (for BS only) powers were measured to calculate the reflection efficiency for mirrors and both the reflection and transmission efficiencies of the BS.

Light from the halogen lamp normally used for transmitted light illumination was first directed through a linear polarizer (#5511, New Focus, San Jose, CA) and band-pass filtered

(HQ605/70M, Chroma). The linearly polarized, filtered light then passed through the condenser, the microscope objective, the filter cube consisting of the same dichroic filter (T565LP, Chroma) and emission filter (HQ605/70M, Chroma) used for normal acquisition, followed by the tube lens, side-port mirror, L2, and an analyzer, to finally strike a power meter placed at the focus of L2. Using the analyzer in the horizontal and vertical positions, the transmitted powers for x- and y- polarizations (at the sample) were measured to find relative transmission efficiency of the optical system (up to L2) as a function of polarization. Multiplying the measured relative efficiencies of each optical element, the final intensity correction necessary for the parallel and perpendicular beam components (G) was calculated. The overall efficiency was confirmed by imaging a pinhole of 50 μm diameter mounted in the field plane between the microscope transmission lamp (IX2-ILL100, Olympus) and the sample. From the image of the lamp in both detection channels, the relative detection efficiency of the parallel and perpendicular detection pathways was calculated.

Comparison of Measured Anisotropy Values with Known Values from Literature

Dilute solutions of RB in water and in 85% glycerol were placed in a sample chamber and illuminated with the 556 nm laser under the same conditions used for acquisition and measurement of the beam profiles, except that the total power at the sample was 8 μW for the RB in 85% glycerol and 25 μW for the RB in water. Images of fluorescence detected with polarization parallel to the laser (Image T, y-polarized) and perpendicular to the laser (Image R, x-polarized) were recorded using the iXon+ camera. The detected fluorescence in images T and R was averaged along a strip 20 pixels wide (~1.7 μm at the sample) passing through the peak of each image of the fluorescence induced by the laser. These profiles were fitted as a sum of two

one-dimensional Gaussians each with center position, width, and amplitude as fitting parameters, as well as a single offset. The amplitudes A_1 and A_2 correspond to the peak intensities in T and R, respectively. The amplitude A_2 was corrected using the relative detection efficiency G=1.23 of the two polarizations[5] (Eq. 10.30, p.299), as determined from direct measurement of the transmission efficiencies of the optical components in the detection pathway (see above). The ratio of corrected amplitudes $\rho = \frac{I_{\parallel}}{I_{\perp}} = G \cdot \frac{A_1}{A_2(1-\chi_{BT})}$ was used to calculate the anisotropy of the solutions, where χ_{BT} = 0.026 accounts for the measured bleed-through of the polarizing beamsplitter at approximately the wavelength of detection. The resulting anisotropy $r = \frac{\rho - 1}{\rho + 2}$ was determined for RB in water to be r_{RBW} = 0.052 ± 0.024, and in 80% glycerol to be r_{RBG} = 0.324 ± 0.025, in agreement with published values from G. Weber,[6] converting from polarization (p) into anisotropy using $r = \frac{2p}{3-p}$.[5] These measurements establish that the method can provide accurate (absolute) anisotropy values within an estimated uncertainty of ±0.025.

Image Analysis

Each image has two regions (T and R), corresponding to light transmitted and reflected by the polarizing beam splitter, respectively. Images of 100 nm fluorescent beads were analyzed to determine the coordinate transformation required (including displacement, linear stretching in x and y, and rotation) to superimpose a chosen region of interest (ROI) in T with the corresponding ROI in R. According to the measurements made, the required additional stretching on a given direction was <10% and the rotations were <6°. The image R is transformed to yield R′, and then the sum of T and R′ is analyzed using standard FPALM single-

molecule localization routines[2,3]. The sum of T and R′ is used to localize molecules rather than the individual images to utilize the total number of detected photons during localizations. Summing the images also recaptures the approximate 2D Gaussian profile of the point spread function whereas the individual images of polarization components are susceptible to ellipticity and other distortions due to probe orientation[7]. Bright objects identified as single molecules by intensity and size thresholding were localized and their positions and intensities determined. The image of each identified molecule was least-squares fitted using a two-dimensional Gaussian. Although the use of high numerical aperture (NA) objectives results in significant deviations from the 2D Gaussian approximation of the point spread function (even for molecules oriented in-plane)[8] and leads to additional positional uncertainty, the use of a slightly lower NA objective (1.2 NA rather than 1.4 NA) helps minimize orientation-induced position-error for Gaussian fits to < 2.5 nm[7]. Quantitatively, the localization precision is calculated using[9]:

$$\sigma_{xy}^2 = \frac{s^2 + q^2/12}{N} + \frac{8\pi s^4 b^2}{q^2 N^2} \qquad \text{(S1)}$$

where σ_{xy} is the precision with which a fluorescent object can be localized in two dimensions, s is the standard deviation of the point spread function, N is the total number of photons collected, q is the size of an image pixel within the sample space, and b is the background noise per pixel. Supplementary Fig. 10 shows the distribution of localization precision calculated from Eq. S1 for each cell appearing in a Figs. 1 and 2 and Suppl. Figs. 9 and 12. For each localized molecule, N was calculated as the product of the 2D Gaussian amplitude and area[2]. For the relatively low noise levels encountered in these experiments, summing the counts in the pixels containing the image of a single molecule to obtain N yields results consistent with the number calculated from the fitted amplitude of the 2D Gaussian. However, statistical analysis of 2D Gaussian fits to simulated molecules show that in general using the fitted amplitude provides a more robust

measure of the number of photons for increasing levels of background noise, whereas summing the pixel counts tends to overestimate (Gould & Hess, unpublished results). For each cell, b was assumed to be constant and taken as twice (due to the superposition of T and R for localization) the standard deviation of a cellular region in T where only background fluorescence (and no PAFP) was visible. Sample stage drift (< 7 nm in x or y over ~20 min.) was characterized previously[2] and was minimal over the relatively short (<5 min.) duration of these experiments (see Suppl. Table 2), compared to the estimated resolution of ~17 nm (see below).

Components of the detected fluorescence parallel ($I_{||}$) and perpendicular ($I_{\perp}$) to the linearly polarized readout lasers were mapped directly to either the direction transmitted ($I_{||}$ for 556 nm readout, $I_{\perp}$ for 488 nm readout) through the polarizing beam splitter, or the direction reflected ($I_{\perp}$ for 556 nm readout, $I_{||}$ for 488 nm readout) by the polarizing beam splitter. To calculate anisotropy values, $I_{||}$ and $I_{\perp}$ were determined by correcting the appropriate detection channel (depending on the readout source) for relative detection efficiency, bleed through of the transmitted channel into the reflected channel, and if applicable, the change in image area due to stretching upon coordinate transformation.

Image Rendering

P-FPALM images were generated by plotting the coordinates of localized molecules as intensity-weighted Gaussian spots of width proportional to the calculated localization precision[2] and colored according to the calculated anisotropy value.

For optimal localization-based resolution, a high density of localized molecules is necessary in addition to precise localization. A modified localization-based resolution can be defined as (Hess et al., Methods in Molecular Biology, accepted)

$$r_L^2 = \sigma_{xy}^2 + r_{NN}^2 \qquad \text{(S2)}$$

where r_L is the localization-based resolution, σ_{xy} is the localization precision (from Eq. S1), and r_{NN} is the nearest-neighbor distance. For example, in Suppl. Fig. 9h, there were 1,136 molecules localized in area of ~ 0.28 μm^2 (conservatively estimating the area of the fiber), which yields a density of ~4,057/μm^2 and an average nearest neighbor distance of ~15.7 nm. For this experiment, the median localization precision was ~7 nm, which yields an effective resolution

$$r_L = \sqrt{\sigma_{xy}^2 + r_{NN}^2} = \sqrt{(7\text{ nm})^2 + (16\text{ nm})^2} = 17\text{ nm} \qquad \text{(S3)}$$

so that the localization precision actually does not limit the resolution, and use of the localization precision alone as an estimate of effective resolution would be improper.

Protocol for Phalloidin Labeling. Approximately 24 hrs after transfection with Dendra2-actin, HAb2 cells were taken out of the incubator and rinsed twice with UV-bleached PBS. The cells were then fixed with 4% paraformadehyde (PFA) for 10 minutes at room temperature (RT) and rinsed twice with PBS. Subsequently the cells were permeabilized with 0.1% Triton X-100 (X-100, Sigma-Aldrich) for 4 minutes at RT and rinsed twice with PBS followed by incubation with 1% bovine serum albumin (BSA; A7906, Sigma-Aldrich) for 20 minutes at RT to minimize non-specific labeling. The cells were then incubated with Alexa-680-phallodin (A22286, Invitrogen) for 20 minutes at RT and rinsed three times with PBS.

Confocal Microscopy of Dendra2-actin Expressing HAb2 Fibroblasts. Hab2 cells were transfected with Dendra2-actin, fixed, permeabilized, and labeled with Alexa-680-phalloidin (see above). Confocal images were taken with an Olympus Fluoview 1000 microscope at room temperature using a 60X 1.42NA oil immersion objective, 488 nm excitation/505-525 nm detection for Dendra2, and 635 nm excitation/655-755 nm detection for Alexa-680-phalloidin. Supplementary Fig. 11 shows results for a cell expressing Dendra2-actin labeled with Alexa-680-phalloidin, demonstrating the degree of colocalization of the two labels for actin. Negligible bleed through was observed from Dendra2 into the phalloidin channel.

Numerical Simulations of Detected Fluorescence from Single Molecules

Calculation of the Detected Fluorescence. A point-like fluorescence emitter with time-dependent dipole moment $\vec{p}(t) = \mathrm{Re}\{\vec{p}_0 e^{i\omega t}\}$ was positioned at location $\vec{r}_P = (x_P, y_P, z_P)$ relative to the coordinate origin (the focus of the objective lens) oriented in direction $\hat{p}$. The radiation pattern of that dipole was calculated using (Born and Wolf 6th Ed., Eq. 13.90, p.651)[10]:

$$\vec{E} = -\left(\frac{\omega}{v}\right)^2 \frac{1}{r^3}\,\vec{r}\times\left(\vec{r}\times\vec{p}\right) \qquad \text{(S4)}$$

where the ratio of angular frequency ω to wave propagation velocity v was defined to be unity and $\vec{r}$ is the vector between the observation point and the dipole position.

The magnitude and direction of the electric field was calculated at a distance of 50 μm from the dipole along rays projecting radially away from the dipole (and toward the objective lens; see Suppl. Fig. 3). For each ray propagating away from the dipole within a cone of angle α measured from the z-axis, the components of the electric field were calculated progressively at each interface using the Fresnel formulae (Born and Wolf, 6th Ed., Eq. 1.20, p.40)[10]:

$$T_{\parallel} = \frac{2n_1 \cos\theta_i}{n_2 \cos\theta_i + n_1 \cos\theta_t} A_{\parallel} \qquad \text{(S5a)}$$

$$T_{\perp} = \frac{2n_1 \cos\theta_i}{n_1 \cos\theta_i + n_2 \cos\theta_t} A_{\perp} \qquad \text{(S5b)}$$

where $T_{\parallel}$ and $T_{\perp}$ are the transmitted electric field components parallel and perpendicular to the plane of incidence, and $A_{\parallel}$ and $A_{\perp}$ are the components of the incident wave parallel and perpendicular to the plane of incidence, respectively, n_1 and n_2 are the indices of refraction of the wave on the incident and transmitted sides of the boundary, respectively, and θ_i and θ_t are the angles between the surface normal of the interface and the incident and transmitted wave propagation vectors, respectively. The new direction of propagation was calculated using the law of refraction. Rays were detected within a cone of angle α=64.2° (1.12 radians) measured relative to the z-axis, yielding a numerical aperture (NA) of 1.2 for the lens (NA= n sin α, where n is the refractive index of the objective immersion fluid, n=1.33 for this case).

The interfaces (see Suppl. Fig. 3) were: water-glass at z=100 μm, glass-water at z=270 μm, and water-lens-air at z=320 μm (where the rays enter the objective lens). The refractive indices used for water and glass were 1.33 and 1.5, respectively. The objective lens was treated as an ideal, thin lens, whereby all rays emitted from the focus of the lens became parallel upon striking the front surface of the lens, and the electric field was calculated using Eqs. S5 for a single surface in the xy-plane. The thickness of the lens was assumed to be negligible, and the light emerging from the lens is assumed to be propagating in air.

The magnitude of the components of the electric field detected from a dipole with orientation $\hat{p}$ and located at $\vec{r}_P$ are integrated separately within a circular aperture at the rear of the lens, each ray weighted by the area subtended in the back aperture:

$$\vec{E}^{det}(\vec{r}_P, \hat{p}) = \int_{\theta=0}^{2\pi} \int_{s=0}^{R_{BA}} \vec{E}(s, \theta, \vec{r}_P, \hat{p}) s ds d\theta \qquad \text{(S6)}$$

where s is the distance from the center of the back aperture (measured perpendicular to the z-axis), and θ is the polar angle in the x-y plane measured from the x-axis. Typically, the circular back aperture is divided into 80 rings spaced evenly as a function of angle measured from the z-axis and 80 evenly-spaced values of θ (6,400 total rays per condition). Increasing the number of rays calculated yielded results equal within three or more digits of precision. The components of $\vec{E}^{det}$ are then calculated as a function of position of the dipole emitter ($\vec{r}_P$) for dipole emitters oriented in the $\hat{x}$, $\hat{y}$, and $\hat{z}$ directions. The detected electric field for an arbitrarily oriented dipole is calculated as an appropriate linear superposition of those detected electric field components. The detected intensity in the parallel ($I_{\parallel}$) and perpendicular ($I_{\perp}$) channels is then proportional to the square of E_x and E_y, respectively. The detected electric field is calculated as a function of dipole position in a grid of 100 μm x 100 μm in the x-y (sample) plane with uniform 0.5 μm spacing in both x- and y- directions, and linearly interpolated for points in between.

Results for a 1.2NA water-immersion objective lens are shown in Suppl. Fig. 4 for dipole-like emitters oriented along the x-, y, and z- axis, for dipole displacements in x and y from 0 μm to +50 μm from the center of the field (focus of the objective). Note the significant rotation of the detected electric field compared to the dipole alignment when the dipole is far (>15 μm) from the center of the field.

Monte-Carlo Simulations of Single-Molecule Emission. Single molecules were distributed randomly within a square area 40μm x 40μm illuminated by an electric field polarized in the x-y plane with a two-dimensional Gaussian intensity distribution with a $1/e^2$ width of 15 μm,

centered at x=y=0, in the focal plane (z=0) of the objective lens. The absorption dipole moment $\hat{p}_{abs}$ of each molecule is oriented using a pseudo-random number generator which on the average produces a uniform angular distribution of unit vectors, or a non-uniform distribution spanning a certain range of angles (see below). For each run, N_{mol} molecules are initially assigned either (A) for PA-GFP, to the inactive (non-fluorescent) state or (B) for rhodamine, to the active (fluorescent) state. During each Monte-Carlo step, the probability of PA-GFP photoactivation P_{PA} is calculated:

$$P_{PA} = P_{PA0} \left| \vec{E}_{illum}(\vec{r}_P) \cdot \hat{p}_{abs} \right|^2 / \left| \vec{E}_{illum}(\vec{r}_P = 0) \right|^2 \qquad \text{(S7)}$$

such that the per-step probability of photoactivation at the origin (focus of the objective) is equal to P_{PA0} when the dipole is aligned with $\vec{E}_{illum}$, the E-field due to the illumination light. Rhodamine molecules are already in the active state, so P_{PA} is by definition zero. The probability of photobleaching of each active molecule is calculated using:

$$P_{PB} = P_{PB0} \left| \vec{E}_{illum}(\vec{r}_P) \cdot \hat{p}_{abs} \right|^2 / \left| \vec{E}_{illum}(\vec{r}_P = 0) \right|^2 \qquad \text{(S8)}$$

where P_{PB0} is the per-frame probability of irreversible photobleaching at the origin for a dipole perfectly aligned with the illumination electric field. Values of P_{PB0}=0 are used to model rhodamine in solution, where the illumination intensity is low, and the rate of photobleaching is therefore negligible. Values of P_{PA0}=0.3, P_{PB0}=0.01 are used for PA-GFP immobilized on glass. All fluorescent molecules are treated as dipole emitters with unit emission dipole moment $\hat{p}_{em}$, which may or may not be aligned with the absorption dipole moment (see below). The detected fluorescence in the parallel and perpendicular channels is calculated using the position and orientation of the dipole, with detected electric field given by

$$\vec{E}_p^{(i)} = [\vec{E}_{illum}(\vec{r}_P^{(i)}) \cdot \hat{p}_{abs}^{(i)}] \, \vec{E}_{det}(\vec{r}_p^{(i)}, \hat{p}_{em}^{(i)}) \qquad \text{(S9)}$$

where $\vec{r}_P^{(i)}$ is the location of the i-th dipole. For mobile molecules at high viscosity, the absorption dipole moment $\hat{p}_{abs}$ is randomized between successive acquisition frames, and the emission dipole orientation $\hat{p}_{em}$ is set equal to that of the absorption dipole. For mobile molecules at low viscosity, the absorption dipole and emission dipole are both randomized independently between each frame. The intensity detected from all active molecules (the fluorescence emission is assumed to be incoherent) in the parallel and perpendicular channels is calculated using:

$$I_{\parallel}^{(i)} = c\left|E_{px}^{(i)}\right|^2 \qquad \text{(S10a)}$$

$$I_{\perp}^{(i)} = c\left|E_{py}^{(i)}\right|^2 \qquad \text{(S10b)}$$

where c is a constant, and i is an index over all active molecules. The measured anisotropy of each molecule is then calculated using

$$r^{(i)} = \frac{I_{\parallel}^{(i)} - I_{\perp}^{(i)}}{I_{\parallel}^{(i)} + 2I_{\perp}^{(i)}}. \qquad \text{(S11)}$$

After 30-200 simulated acquisition frames, the molecules are re-initialized and the next run is commenced. From the values of anisotropy for each molecule, an intensity-weighted histogram of anisotropies is calculated.

Simulation results for dye in solution (randomly oriented, N_{mol}=50,000) are shown for the low-viscosity and high-viscosity limits (Suppl. Fig. 6a). In the low-viscosity limit, molecules reorient rapidly before emitting fluorescence, resulting in a complete loss of the initial polarization direction, and emission with zero mean anisotropy (r_{ave}=0.0016). In the high-viscosity limit, molecules do not reorient before emitting, leading to emission from a dipole

emitter oriented parallel to the excitation transition dipole moment, and positive mean anisotropy (r_{ave}=0.4002) in agreement with predictions from analytical theory. Importantly, these simulations take into account the rotation of the electric field vector resulting from passage through the media, coverslip, immersion liquid, and objective lens. Simulated anisotropy histograms for PA-GFP immobilized on glass (Suppl. Fig. 6b) agree fairly well with the measured histogram for 22,476 molecules using: two-dimensional circular Gaussian beam illumination $1/e^2$ radius r_0=12 μm, N_{mol}=22,476 total molecules distributed randomly over a 10μm x 10μm square area, 30 frames per acquisition, and two populations of molecules. The first population of 7,417 molecules had an orientation of 15° relative to the z-axis and an angle of φ=51±16° measured from the x-axis. The second population of 15,059 molecules also had an angle of 15° relative to the z-axis and an angle of φ=27±12° measured from the x-axis in the x-y plane. These populations and orientations are not necessarily the unique or best description of the measured histogram. The measured anisotropy histogram was not well-described by a single population or by two populations of molecules with random orientation.

P-FPALM Images of Hemagglutinin (HA)

Supplementary Fig. 15 shows anisotropy values for PA-GFP-HA in fixed fibroblasts. The spatially heterogeneous distribution of molecules includes one cluster close to the edge of the cell which has particularly low (close to zero or negative) anisotropy values. Supplementary Figs. 16-17 show anisotropy values for Dendra2-HA in fixed fibroblasts. Due to the favorable photophysics of Dendra2 (reduced readout-induced activation, data not shown), the Dendra2-HA construct could be imaged at a higher density. The clustered distribution of HA reveals a heterogeneous distribution of single molecule anisotropies. Comparing small clusters (Fig. 16),

differences in anisotropy value are sometimes observed, but these cluster-to-cluster differences are much more obvious when larger clusters (Fig. 17) are compared.

Assembly of HA molecules into membrane clusters is important for both entry of the influenza virus into host cells by cooperatively mediating membrane fusion[11] and for budding of new viruses from host cells, which occurs from liquid ordered membrane (raft) domains.[12] Relative orientation of HA molecules could certainly be an important mediator of cooperativity in membrane remodeling processes. The large range in sizes of HA clusters is consistent with findings from electron microscopy[13] and previous FPALM imaging[2].

Error in Anisotropy Values Measured Using High NA Optics

Unambiguous measurement of the three dimensional orientation of a single molecule can be accomplished by detecting the fluorescence emission polarized along three different directions[14]. The anisotropy values presented here, measured with two polarizations, provide a reasonable approximation of the anisotropy while maintaining a good signal to noise ratio. The mixing of fluorescence emitted parallel and perpendicular to the excitation source increases significantly as dipole orientation approaches alignment parallel to the optical axis, although the thresholding inherent to localization-based imaging also results in low probabilities of detection of molecules that are closely aligned to the optical (z-) axis and weakly excited.

Using the methods described above, the detected intensities in the parallel and perpendicular channels were determined as a function of probe position and orientation near the center of the field in the x-y (focal) plane. The detected intensity was calculated from the electric field outside the back aperture of the objective lens (Eq. S6):

$$I_{\parallel}^{det}(\vec{r}_P,\hat{p}) = \int_{\theta=0}^{2\pi}\int_{s=0}^{R_{BA}} \left|E_x(s,\theta,\vec{r}_P,\hat{p})\right|^2 s\,ds\,d\theta \qquad \text{(S12a)}$$

$$I_{\perp}^{det}(\vec{r}_P,\hat{p}) = \int_{\theta=0}^{2\pi}\int_{s=0}^{R_{BA}} \left|E_y(s,\theta,\vec{r}_P,\hat{p})\right|^2 s\,ds\,d\theta \qquad \text{(S12b)}$$

and from the parallel and perpendicular intensities, the anisotropy was calculated using Eq. S11. The dipole axis unit vector was oriented with angle Θ relative to the z-axis and angle Φ relative to the x-axis measured in the x-y plane. Values of the anisotropy were calculated for Θ=0 to 90° and Φ=0 to 90° in 2° increments. The intensities in Eqs. S12 take into account the tipping of the electric field by the high-NA objective, as well as effects from the water-coverslip, coverslip-water, and water-objective interfaces. The expected (calculated) detected anisotropies are shown as a function of probe orientation in a color-coded plot (Suppl. Fig. 5) and demonstrate that despite the rotation of the polarization by the objective lens, a particular anisotropy value measured at a particular location close to the center of the field corresponds to a certain set of probe orientations. While a measurement of a single anisotropy value will not decisively identify the exact orientation of the probe in three dimensions, the anisotropy value does provide useful information about which orientations the probe could have. Small displacements (< 7 μm) from the center of the field result in variability of less than 0.01 in anisotropy at any given Θ or Φ value. Two molecules with anisotropy values different by more than the experimental uncertainty are therefore in different orientations.

Measurement of the Aniostropy Histogram of Caged Fluorescein in Agarose

Agarose (A-7431, Sigma) was dissolved (1% by weight) in UV-treated PBS, shaken to mix, heated for 40 seconds in a microwave on high power, shaken again to mix, then heated to

boiling temperature. In a darkened room, 200 μL of the hot agarose solution was pipetted into a NUNC well, into which 2 μL of 2 μM caged fluorescein (C20050, Invitrogen) in PBS was immediately added and mixed by repeatedly drawing and expelling half of the mixture with a P1000 pipetman. The mixture was allowed to cool and congeal, then imaged by P-FPALM at room temperature with 488 nm readout excitation.

Simulation of the Anisotropy Histogram of Caged Fluorescein in Agarose

Molecules of caged fluorescein were described by Monte-Carlo simulation as rotating dipoles at the center of the field, in the focal plane of the microscope. Methods described above were used to calculate the detected intensity in the parallel and perpendicular channels (Eqs. S12) given the orientation of the dipole at any particular time, taking into account the rotation of the detected polarization due to the high-numerical objective, water-coverslip, and coverslip-water interfaces. Fifty thousand (50,000) molecules were individually simulated. Each molecule was simulated for 40,000 Monte-Carlo (MC) steps. During each step the molecule had a finite chance (the success of which was simulated by a random number generator) of rotating slightly (±2° in theta, ±2° in phi, 0.004 probability per MC step) or completely randomizing its orientation (0.004 probability per MC step). The molecules were assumed to be in the active state initially, and the probability of excitation was given by a constant times the dot product between the electric field unit vector (linearly polarized in the x-direction) and the dipole unit vector squared. Given that the molecule was excited, the probability of irreversible photobleaching during that step was calculated using Eq. S8 with $P_{PB0} = 0.0008$. The probabilities of emission in the parallel and perpendicular channels, respectively, were calculated as a constant times the detected intensity in the parallel and perpendicular channels, for a dipole

with the same orientation as the transition dipole of the molecule (Eqs. S12). Thus, per MC step, each active molecule could rotate, could emit one or zero photons in the parallel channel, could emit one or zero photons in the perpendicular channel, and could potentially photobleach. The image of each molecule was simulated by distributing the photons in the parallel channel and perpendicular channels separately as a Gaussian with width equal to the point spread function, centered at the origin of a 7x7 box (one box for the parallel channel, one box for the perpendicular channel, the same dimensions used to analyze the experimental data). The number of photons in the parallel and perpendicular images were used for the values of $I_{\parallel}$ and $I_{\perp}$, respectively, to calculate the single-molecule anisotropy in Eq. S11. The histogram of anisotropy values was then calculated for all molecules with at least one pixel in either image above a threshold T_1=40 photons.

Supplementary Fig. 7 shows comparison of the measured anisotropy histogram for caged fluorescein in agarose and the simulated histogram. Other than a shift of the measured anisotropy histogram by ~0.04 toward smaller values compared to the calculated histogram, reasonable agreement between the two is observed. This shift is slightly larger than the accuracy estimated from measurements in solution of non-photoactivatable fluorophores, but is likely due to slight errors in the estimation of the background levels, which were significantly higher in the agarose gel than were normally observed in cells. Increased background causes lower anisotropy values because it contributes to both parallel and perpendicular channels equally, thereby leading to a larger denominator in Eq. 1, while the numerator in Eq. 1 remains unchanged. Nonetheless, the profile of the two histograms is in good agreement, and the peak anisotropy value for a single photoactivatable fluorescent molecules is close to that expected from theory, again demonstrating the validity of the method.

References

1. Patterson, G.H. and Lippincott-Schwartz, J., *Science* **297**, 1873-1877 (2002).
2. Hess, S.T., Gould, T.J., Gudheti, M.V., Maas, S.A., Mills, K.D., and Zimmerberg, J., *Proc. Natl. Acad. Sci. U. S. A.* **104**, 17370-17375 (2007).
3. Hess, S.T., Girirajan, T.P., and Mason, M.D., *Biophysical Journal* **91**, 4258-4272 (2006).
4. Juette, M.F., Gould, T.J., Lessard, M.D., Mlodzianoski, M.J., Nagpure, B.S., Bennett, B.T., Hess, S.T., and Bewersdorf, J., *Nature Methods* **5**, 527-529 (2008).
5. Lakowicz, J.R., *Principles of fluorescence spectroscopy*, 3rd ed. (Springer Science, New York, 2006).
6. Weber, G., *Journal of the Optical Society of America* **46**, 962-970 (1956).
7. Enderlein, J., Toprak, E., and Selvin, P.R., *Optics Express* **14**, 8111-8120 (2006).
8. Bartko, A.P. and Dickson, R.M., *Journal of Physical Chemistry B* **103**, 11237-11241 (1999).
9. Thompson, R.E., Larson, D.R., and Webb, W.W., *Biophysical Journal* **82**, 2775-2783 (2002).
10. Born, M. and Wolf, E., *Principles of optics : Electromagnetic theory of propagation, interference and diffraction of light*, 6th ed. (Cambridge University Press, Cambridge, UK, 1997).
11. Ellens, H., Bentz, J., Mason, D., Zhang, F., and White, J.M., *Biochemistry* **29**, 9697-9707 (1990).
12. Scheiffele, P., Rietveld, A., Wilk, T., and Simons, K., *Journal of Biological Chemistry* **274**, 2038-2044 (1999).
13. Hess, S.T., Kumar, M., Verma, A., Farrington, J., Kenworthy, A., and Zimmerberg, J., *Journal of Cell Biology* **169**, 965-976 (2005).
14. Fourkas, J.T., *Optics Letters* **26**, 211-213 (2001).